Measurement of Strain Localization Resulting from Monotonic and Cyclic Loading at 650 °C in Nickel Base Superalloys

**J. C. Stinville[1] · M. P. Echlin[1] · P. G. Callahan[1] · V. M. Miller[1,4] · D. Texier[3] ·
F. Bridier[2] · P. Bocher[3] · T. M. Pollock[1]**

Abstract A methodology is presented for the use of the oxide scale that develops in polycrystalline Ni-base superalloys at service temperature, as a speckle pattern for µm-scale resolution strain measurements. Quantitative assessment of the heterogeneous strain field at the grain scale is performed by high-resolution SEM digital image correlation under monotonic and cyclic loading in polycrystalline Ni-base superalloys up to 650 °C. In the René 88DT superalloy, strain localization is observed near twin boundaries during low cycle fatigue (LCF) at intermediate temperatures, correlating with activation of $\{111\}\langle 110\rangle$ and $\{111\}\langle 112\rangle$ slip systems. A strong correlation between the microstructural configuration that promotes strain localization during monotonic loading and crack initiation at 650 °C in low cycle fatigue was observed.

✉ J. C. Stinville
stinville@engineering.ucsb.edu

✉ M. P. Echlin
mechlin@engineering.ucsb.edu

[1] Materials Department, University of California Santa Barbara, Santa Barbara, CA, USA

[2] DCNS Research, DCNS, Bouguenais, France

[3] Department of Mechanical Engineering, Ecole de Technologie Supérieure, Montréal, Québec, Canada

[4] Materials Science and Engineering Department, North Carolina State University, Raleigh, NC, USA

Keywords High resolution digital image correlation · Polycrystalline superalloy · Rene88DT · Strain localization · High temperature fatigue

Introduction

Damage during cyclic loading of polycrystalline metallic alloys used for turbine disk components involves the accumulation of plastic strain at the scale of individual grains, particularly in the vicinity of grain boundaries and interfaces. For example, Miao et al. [1, 2] reported for the nickel-base alloy René 88DT under very high cycle fatigue (VHCF) loading at room temperature that cracks initiated in high Schmid factor grains for the $\{111\}\langle 110\rangle$ slip system, parallel to and slightly offset from coherent twin boundaries. The microstructural features that localize strain and initiate fatigue damage change between room temperature and turbine component service temperatures, due to a shift in the deformation mode [3, 4]. For example, at intermediate temperatures in nickel-base alloys, the secondary slip system $\{111\}\langle 112\rangle$ becomes active [3, 4]. There is a need for quantitative assessment of the heterogeneous strain fields at the microscopic scale for the development of predictive models of monotonic and cyclic loading at component service temperatures and to better relate the local mechanical behavior to the global loading conditions. Crystal plasticity simulations based upon either molecular dynamics or finite elements are currently being developed to address these microstructural-influenced phenomena [5–8] and localization of plasticity along slip bands or persistent slip bands [9]. Experimental data on strain localization obtained via *in situ* scanning electron microscope (SEM) digital image correlation (DIC) is available [10–18] at the microscale, however few experiments [19–21] have resolved strain fields at the scale of the localization of plasticity (slip bands). Recent studies [19, 20, 22–25] show that by minimizing or correcting the complex SEM imaging distortions [19, 22], it is possible to obtain the necessary spatial resolution to measure micrometer and sub-micrometer strain fields at room temperature where plasticity and slip localizes [19, 20, 22, 23, 26–28]. Such information will allow for direct comparison with elastic and crystal plasticity simulations and ultimately support the development of improved models for life prediction.

Engineered polycrystalline superalloys are operated under oxidizing conditions at intermediate and high temperatures with superimposed cyclic loading. High-resolution SEM DIC procedures that have yielded new insights into the deformation processes at room temperature need to be developed for elevated temperature investigations. Here we present an advanced sub-grain DIC technique applied to nickel base superalloys with average grain size below 50 µm to observe the straining processes at the sub-grain scale during monotonic and cyclic loading at temperatures up to 650 °C. The new approach employs *ex-situ* testing and the stable oxide layer that forms during thermal exposure as the DIC speckle pattern for the investigation of strain localization during plasticity at temperatures up to 650 °C in the low cycle fatigue (LCF) regime.

Experimental Materials

Three commercially available polycrystalline nickel-base superalloys used for turbine disk applications were investigated in this research: René 88DT, Inconel 718DA and IN100. All these alloys have grain sizes that are between 10-50 µm and contain multiple size populations of one or more strengthening phases (indicated as γ' and γ''), which grow from solution and in subsequent aging steps [29]. The unique attributes of each alloy are described presently. The grain structure of each alloy is displayed in Fig. 1 using electron backscatter diffraction (EBSD) measurements.

The polycrystalline powder metallurgy processed nickel-base superalloy, René 88DT, has a nominal composition of 13Co, 16Cr, 4Mo, 4W, 2.1Al, 3.7Ti, 0.7Nb, 0.03C, 0.015B (wt%) [30]. The microstructure of the alloy consists of a γ matrix and two populations of γ' precipitates: larger secondary and nm-scale tertiary γ' within the γ grains [30]. The size of the secondary γ' phase is about 100-200 nm, while tertiary γ' precipitates are several nanometers in diameter. Crystallographic features have been previously studied using EBSD measurements [31] showing that the material possesses very weak crystallographic texture, a large population of $\Sigma 3$ boundaries (58% by 2D measurements and 70% by 3D measurements of the total boundary fraction [32]), an average grain size of 26 µm, and a low fraction of large grains on the order of two to five times of the average grain size.

The direct aged Inconel 718 (IN718DA) material used in this study was extracted from a forged bar. The nominal composition of this alloy is 0.14Co, 17.97Cr, 0.023C, 0.0062N, 17.3Fe 0.56Al, 1Ti, 5.4Nb, 0.03C (wt%) [33]. A hardened primary (γ') and secondary (γ'') direct-aged microstructure results from the aging heat treatment step applied directly after the forging operations with a grain size of 25 µm. The size of the primary γ' phase is about 60 nm, while secondary γ'' precipitates display a disk-like shape with several nanometers in diameter.

The IN100 material was also powder metallurgy processed, having a composition of 12.4Cr, 18.5Co, 4.7Ti, 5.5Al, 3.2Mo, 0.8V and 0.07C (wt%). The average grain size of the IN100 material is 49 µm. The material contains primary, secondary, and tertiary γ' precipitates that form during cooling and aging steps, as previously observed [34, 35]. Grain boundaries are decorated with primary µm-scaled irregular shaped γ'. Cooling induced γ' particles with the form of ogdoadically-diced cubes are also visible in each γ grain.

Mechanical Testing and Sample Preparation

Monotonic testing was performed on the René 88DT material in air at 650 °C on a electromechanical machine in stress control mode at various maximum tensile stresses ranging from 800 MPa to 1025 MPa. Cyclic testing was performed in air at 400 °C and 650 °C in the low cycle fatigue (LCF) and high cycle fatigue (HCF) regimes. Fatigue tests were performed in a symmetric, uniaxial, push-pull mode on an electromechanical machine at various maximum stresses raging from 758 MPa to 1000 MPa, with a R-ratio of -1 or -0.5 and a frequency of 1 Hz. Cylindrical dogbone-shaped

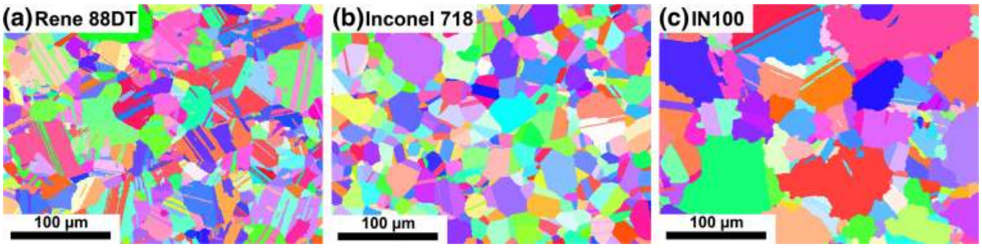

Fig. 1 Electron backscatter diffraction maps show the microstructure of the (**a**) René 88DT, (**b**) IN718DA and (**c**) IN100 superalloys

specimens with a gauge diameter of 5 mm and gauge length of 16 mm were used in this study. The samples were heated using an induction coil and the testing temperature was controlled within ±10 °C along the gauge section of the fatigue specimens using a calibrated infrared pyrometer.

Sub-grain scale DIC measurements were made at different percentages of the fatigue lifetime following the methodology in Fig. 2. Sub-grain scale DIC refers to the strain measurements at the scale that is approximately 1/10 the grain size or lower. The grain orientations from the DIC measurement areas were collected using EBSD. Thermal treatments of the samples, at temperatures of 400 °C or 650 °C, were performed over a 12 hour period prior to cyclic deformation with heating and cooling rates of 10 °C min^{-1}. The thermal treatments result in a fully developed oxide layer at the sample surfaces in all of the polycrystalline nickel base superalloys investigated [3, 36–42]. SEM images were acquired prior to mechanical deformation, establishing the unstrained DIC base measurement. Thereafter, samples were heated to temperatures of 400 °C or 650 °C for 2 hours to form a stable oxide on the sample surfaces, as described in more detail in Section “Development and Validation of a DIC Technique for use at 650 °C”, after which cyclic deformation was performed. These fatigue experiments were interrupted after 1-10 cycles and then at 20% and 95% fatigue life. The interrupted experiment samples were cooled to room temperature and SEM images were collected from the same location as those of the unstrained samples.

DIC analyses were then performed on the sets of SEM images captured at different numbers of fatigue cycles in order to determine the in-plane residual plastic strain field at the sample surface using the methodologies developed and described in more detail elsewhere [23]. The stable oxide layer that forms during the initial, deformation-free, thermal treatment provides secondary electron SEM contrast that is used by the DIC algorithms to track displacements and ultimately measure strain fields at the sample surface. The crack densities and fatigue lifetimes for samples tested with or without interruptions were indistinguishable for the specimens tested.

EBSD and sub-grain DIC measurements require flat specimens, therefore two flat areas 2.5 mm in width and 8 mm in length were machined into the opposite sides of the gauge section of selected fatigue specimens, shown

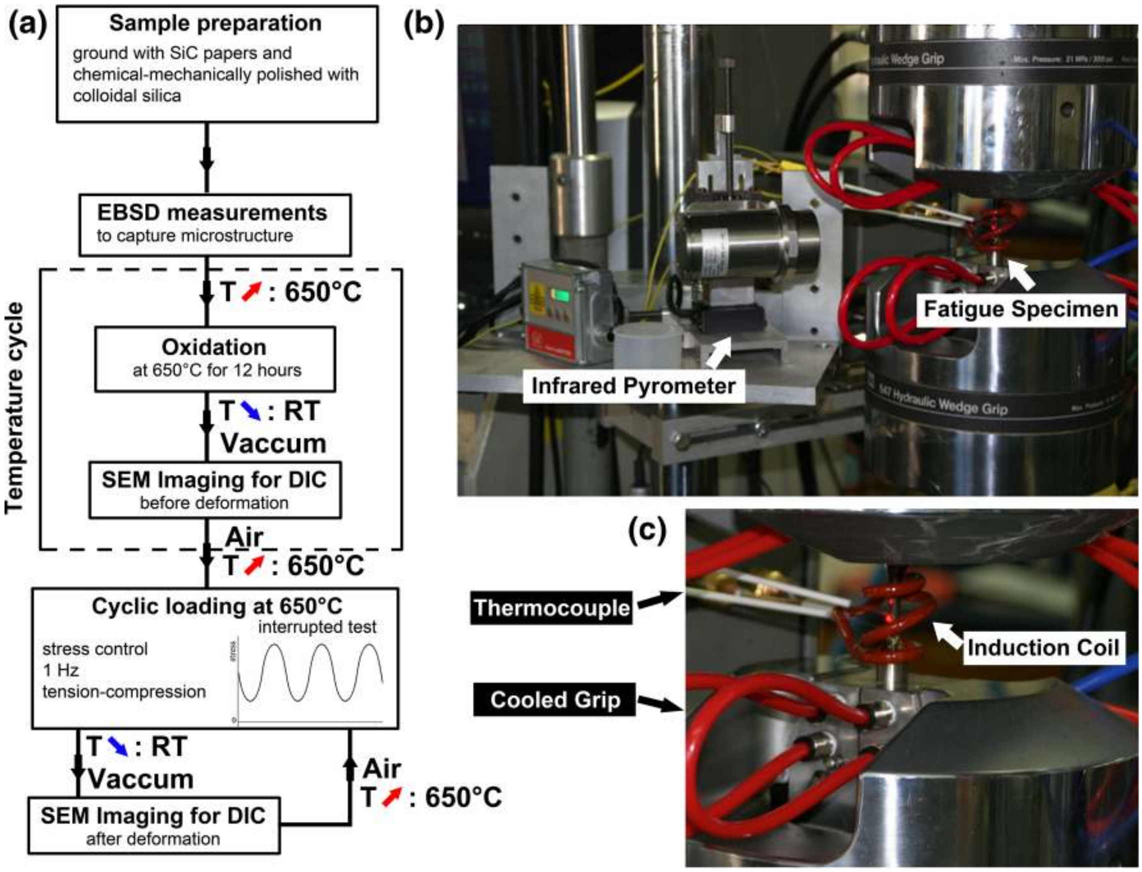

Fig. 2 The flow chart in (**a**) shows the methodology for sample preparation, EBSD data collection, and SEM DIC collection before and after thermomechanical cycling. Initially the samples were exposed to thermal cycles without mechanical deformation to form a stable oxide and baseline SEM DIC image set. Subsequently, a sample is fatigue cycled with periodic interruptions to measure the residual strain field with SEM DIC. The thermomechanical fatigue setup including the induction coil heater and laser extensometer is shown in (**b**) and (**c**)

in Fig. 3. The geometry of the flat areas was designed to limit stress concentrations due to machining. The flat areas were also mechanically polished to further reduce any local deformation and damage. The specimens were ground with SiC abrasives and chemical-mechanically polished with 0.05 µm colloidal silica for 12 hours to remove any residual surface deformation. The polishing procedure consisted of polishing the gauge section of the sample with a cylindrical SiC abrasive tube, while the sample was rotated, using an in-house polishing system. The head of the fatigue specimen was clamped into the polishing system whereby a fast linear motion of the SiC abrasive was applied during slow rotational motion of the sample. The specimens with and without the machined flats exhibited crack densities and fatigue lifetimes that were indistinguishable from each other [27].

SEM and EBSD Measurements

EBSD maps were acquired prior to deformation with an EDAX Hikari XP detector with a step size of 0.5 μm. SEM imaging for sub-grain DIC measurements was performed at room temperature *in-situ* in a FEI Helios FEG focused ion beam (FIB-SEM) system on the flats of the fatigue specimens after unloading. In order to minimize distortion errors inherent to SEM imaging [19, 22], SEM parameters were chosen following the guidelines of Kammers and Daly [19, 22] and Stinville et al. [23]. SEM images were collected at horizontal field widths (HFWs) of 85 µm, with 0.34 nA electron beam current, and a 20 µs dwell time (6 minutes per image). These parameters were selected to reduce both drift and spatial distortions [19, 22]. An electron beam acceleration voltage of 5 kV was used to minimize charging effects and reduce beam drift. A short working distance of 5 mm was used to obtain higher spatial imaging resolution and electron beam stability. These parameters are outlined in more detail elsewhere [23] and yield strain errors due to drift distortion, beam defects and secondary electron detector noise that are below 0.15%. At horizontal field widths (HFWs) of 85 µm, spatial distortion induced strain errors are less than 0.05% [23].

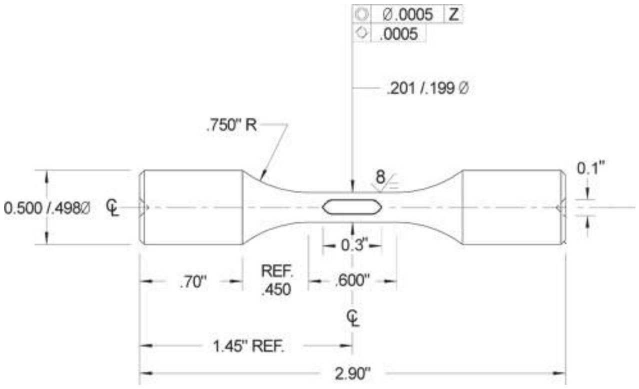

Fig. 3 The mechanical drawing of the fatigue sample type used for testing is shown. SEM DIC and EBSD images were collected from the machined and polished flat region in the center of the schematic

Digital Image Correlation

The in-plane displacement fields at the microscopic scale were obtained using the commercial software VIC 2D 2009 [43]. The software parameters used include a zero-normalized squared-difference correlation criterion for correlation and a 5 × 5 subset decay kernel matrix (minimum decay filter available) for deriving strain values [44]. The SEM images (4096 × 3775 pixels) were divided into custom-sized subsets ranging from 9 × 9 to 101 × 101 pixels regularly spaced by a step size in both the horizontal and vertical directions. A subset size of 21 × 21 pixels (0.4 × 0.4 µm) was used for all the strain maps shown in the this article. All DIC calculations were made using a step size of 5 pixels (104 nm). DIC measurements were constructed by comparing secondary electron images from each deformation step to images of the undeformed specimen.

Development and Validation of a DIC Technique for use at 650 °C

Oxide Layer Speckle Pattern

The passive oxide layer that grows on the surface of nickel base superalloys provides a stable DIC speckle pattern for the measurement of the strain field at the sample surface during fatigue deformation at temperatures up to 650 °C. Variability in the thickness and chemistry of the oxide generated above γ and γ' phases at the sub-micrometer scale provides a mechanism for the secondary electron imaging contrast [23]. In order to perform SEM DIC measurements using the oxide speckle pattern, the evolution, stability, and adhesion of the oxide formed at elevated temperature on nickel base superalloys during thermal-mechanical exposure and fatigue deformation were also investigated.

Oxide Layer DIC Correlation

The speckle pattern used for DIC was formed by oxidation in air of each of the three alloys at 400 °C or 650 °C for 12 hours. SEM images and EBSD maps of the oxidized sample surface for René 88DT are shown in Fig. 4 for DIC measurements made from samples cycled in fatigue at 400 °C and 650 °C. The speckle pattern contrast results from the oxide structure and is directly related to the circular

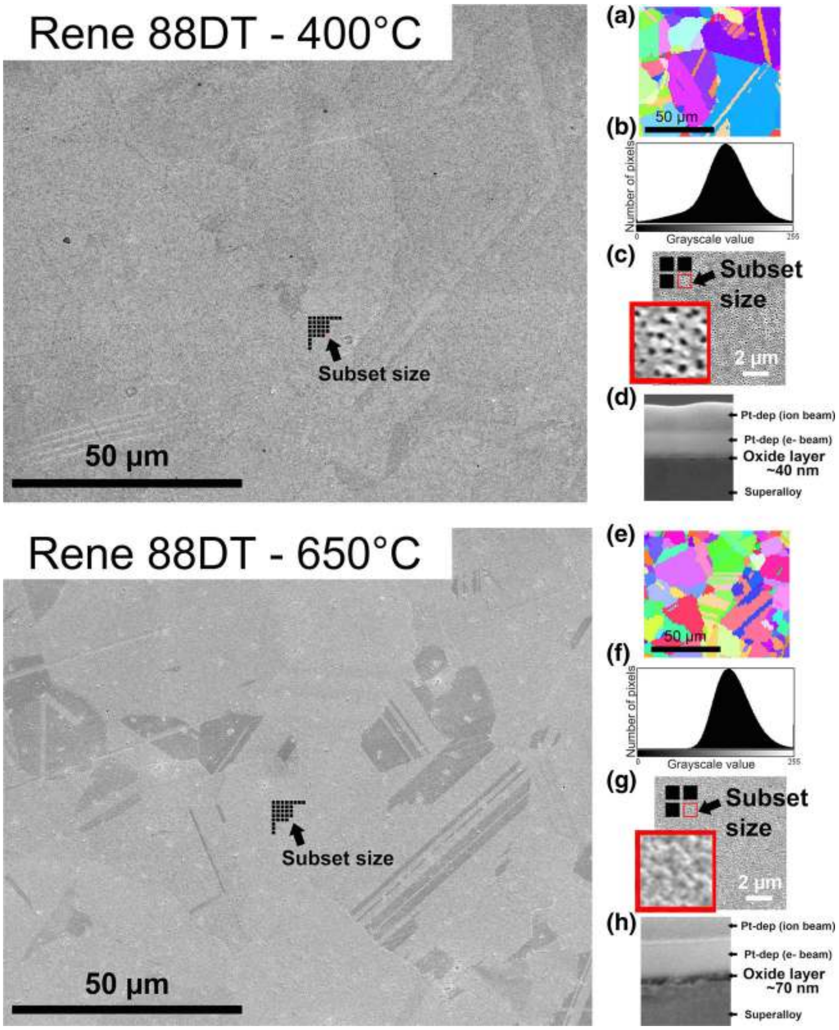

Fig. 4 SEM images show the oxidized surfaces of René 88DT at 400 °C and 650 °C, with the DIC parameter, subset size, inset within the images. EBSD maps were collected from the SEM DIC imaging fields, in (**a**, **e**), with the fine twin structure resolved. The microstructural contrast resulting from the chemical variation between the oxides that form above the γ and γ' phases is shown in (**c**, **g**), which provide a high contrast speckle pattern as shown in the histogram in (**b**, **f**). FIB-SEM cross sections of the oxide surface show the 40-70 nm oxide layer that is adhered to the superalloy substrate surface (**d** ,**h**)

shaped secondary γ' precipitates, as shown for IN100 and IN718DA, Fig. 5. The red and black boxes in Figs. 4(c) and 5(c) indicate the optimized subset size, 21 × 21 pixels (0.4 × 0.4 µm), relative to the microstructure used for DIC measurements.

A FIB-SEM microscope was used to make cross sections from the oxide layer resulting from 12 hours thermal exposure at 400 °C and 650 °C. A 5kV accelerating voltage was used to perform the final gallium ion beam cleaning cuts at 0.1 nA current. The micrographs in Figs. 4(d) and 5 show the platinum cap, the oxide layer, and the nickel base superalloy substrate for the three alloys. As reported in the literature for these temperatures [36, 38, 39], the oxide layers are very thin ranging from 30-100 nm. The oxide formed at 400 °C in René 88DT has a high contrast speckle pattern that consists of dark circles (precipitates) of contrast surrounded by gray values, as shown in the inset in Fig. 4(c) and the histogram Fig. 4(b). The light areas are Cr-rich oxide regions that form due to Cr enrichment in the γ matrix compared to the γ' precipitates [36, 38, 39]. At 650 °C the contrast of the speckle at the surface of the sample is attenuated, forming a more diffuse gray distribution due to a more mixed oxide composition.

The use of SEM imaging for DIC comes at the cost of complex image distortions, which affect the strain measurement resolution. Previous research on samples strained at room temperature [23] has shown that the strain measurement resolution depends on the horizontal field width (HFW) of the acquired images, the correlation parameters for DIC (subset size, step size and strain windows size) and the speckle pattern. A optimal HFW of 85 µm was used to minimize the spatial and drift distortion [23]. Optimization of the DIC parameters has been performed for the speckle patterns at 400 °C and 650 °C in nickel based superalloys by collecting unstrained image pairs from oxidized sample surfaces as a function of exposure at elevated temperature. The standard deviation in strain as a function of the subset size in nanometers is shown in Fig. 6 for room temperature [23], 400 °C and 650 °C. The strain measurement resolution is best for the 650 °C experiments, compared to 400 °C or room temperature, due to imaging contrast mechanisms in the speckle patterns.

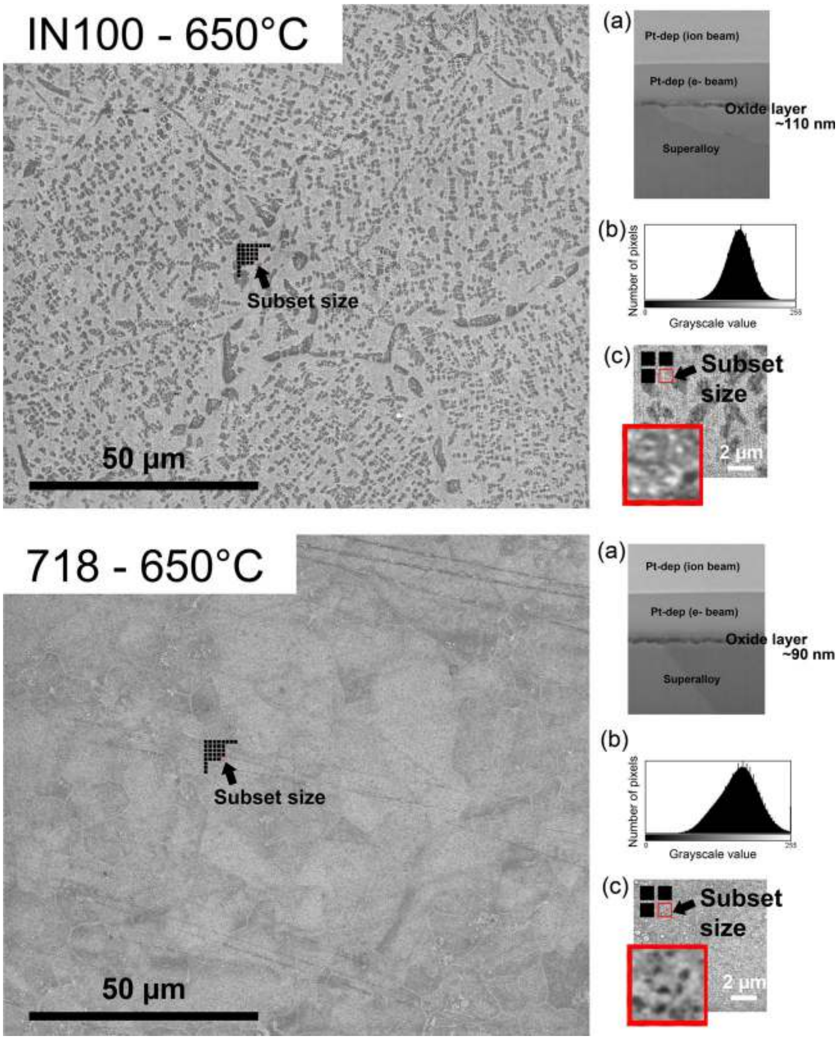

Fig. 5 SEM images from the oxidized surface of the polycrystalline superalloys IN100 and IN718DA show the microstructural contrast resulting from the chemical variation between the oxides that form above the γ and γ' phases and the SEM DIC parameter, subset size. The contrast formed between the two phases is shown at higher magnification in (**c**) which provide a high contrast speckle pattern as shown in the histogram in (**b**). FIB-SEM cross sections of the oxide surface (**a**) show the 90-110 nm oxide layer that forms on each of these alloys at 650 °C

Temperature Dependent Oxide Evolution

Nickel base superalloys maintain a protective surface oxide scale during high temperature exposure [3, 36–42]. This protective scale is composed of chromia and alumina oxides that grow slowly, are stable, are adherent to the substrate, and are free of cracks and pores. A temperature-dependent minimum level of aluminum and chromium alloying content is necessary for the formation of a continuous protective surface scale.

Chromium oxide is the predominant phase that evolves in commercial turbine disk superalloys, such as IN100,

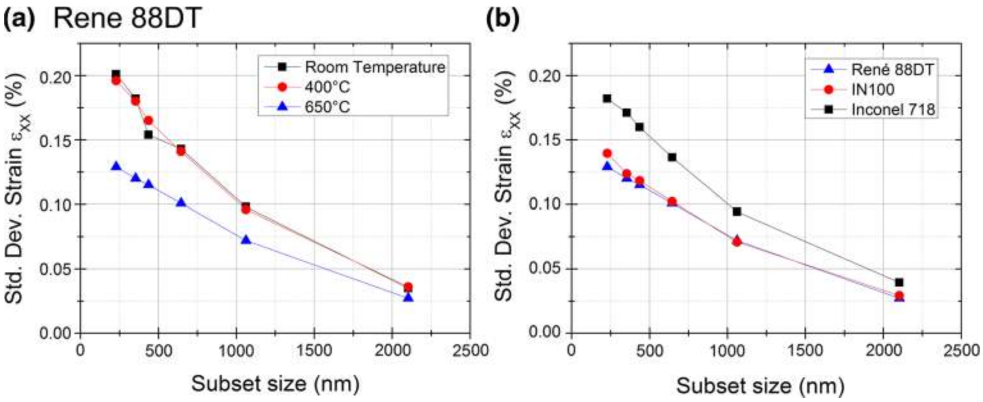

Fig. 6 The variability in ϵ_{xx} measured in René 88DT decreases with larger subset size, resulting in coarser spatial strain field resolution (**a**). At 650 °C, the variability in ϵ_{xx} with subset size follows a similar trend for all three superalloys, with slightly higher variability in IN718DA

Inconel 718DA and René 88DT, at temperatures up to 800 °C. However nickel, aluminum, and iron oxides can be present in small amounts [3, 36–42]. At temperatures below 650 °C, the oxide layer is very thin, as shown in Figs. 4 and 5, and suitable for sub-grain SEM DIC. However, there are limitations to the use of the oxide layer as a speckle pattern with increasing temperature. SEM images of the surface and FIB-SEM cross-sections into the depth of the oxide scale, are shown in Fig. 7, for oxidation at temperatures of 750, 850, 950, and 1050 °C in René 88DT for 12 hour exposures. Energy dispersive x-ray spectroscopy (EDS) was used to characterize these scales and at 750 °C the oxide layer consists of chromia as observed at 650 °C, however internal oxidation has begun to occur, especially at grain boundaries, Fig. 7. At 850 °C and 950 °C, the external scale consists mainly of chromia and titanium dioxide with some minor transition oxides. Additionally, granular rutile titania was observed to form at the surface. A layer of titanium dioxide was also observed to form below the chromium oxide layer. The total thickness of the external oxide scale was found to be several hundreds of nanometers. At 1050 °C, the chromia evaporates and granular rutile crystals fully cover the surface. At a temperature of 850 °C and above, the amount of internal oxidation becomes significant. This internal oxide layer is composed of titanium dioxide and alumina, which develops below the external oxide scale with alumina forming deeper into the substrate. At temperatures above 850 °C, the extent of internal oxidation and the external scale precludes the SEM DIC strain measurements from being representative of the deformation occurring in

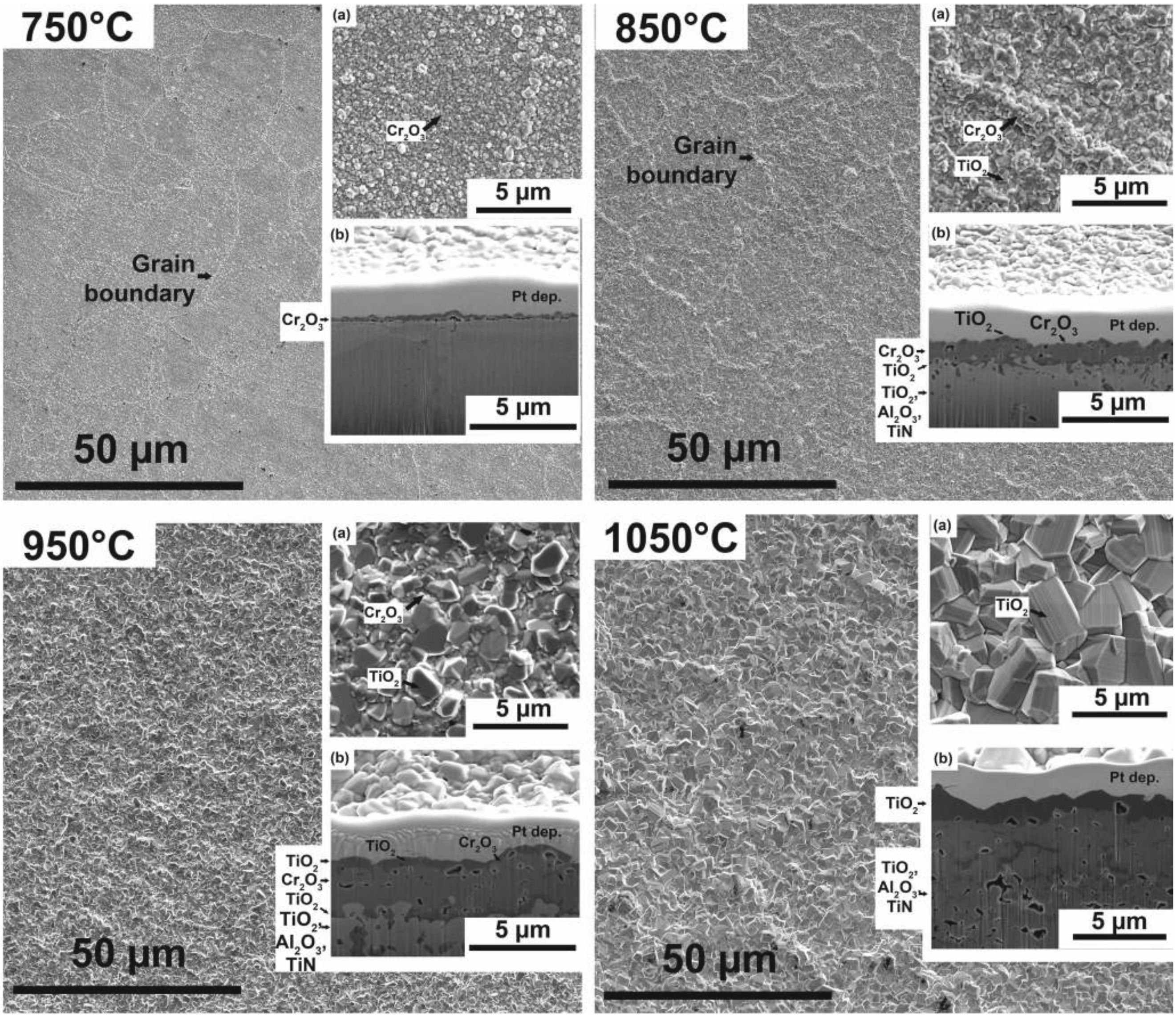

Fig. 7 The oxides forming at the surface of René 88DT at 750, 850, 950, and 1050 °C, with higher magnification inset (**a**), and FIB-SEM cross sections (**c**) Internal oxidation is observed for materials oxidized at temperatures above 850 °C

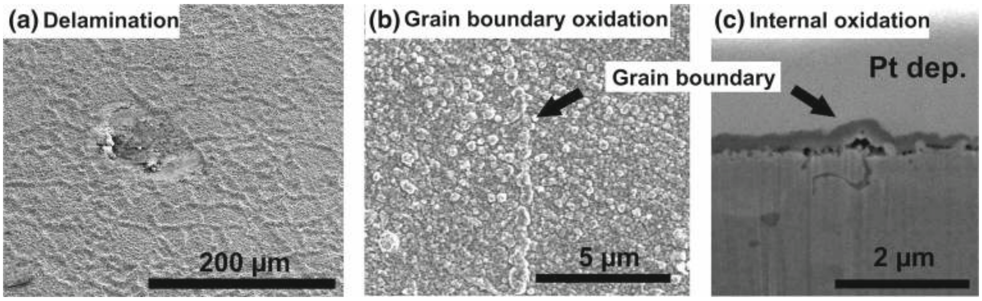

Fig. 8 SEM images of (**a**) oxide layer delamination that occurs during thermal cycling at 950 °C in air, (**b**) preferential oxidation at the grain boundary at 750 °C and (**c**) internal oxidation at 750 °C

the substrate. Several other limitations exist at temperatures above 750 °C, such as oxide delamination or spallation, which is likely to occur during thermal cycling, as shown in Fig. 8(a). Oxidation can also occur preferentially at the grain boundaries, Fig. 8(b), producing roughness at the sample surface that is not favorable for SEM DIC. Moreover, internal oxidation occurs preferentially at grain boundaries in Fig. 8(c), thereby decoupling the mechanical response of the oxide from that of the substrate. Fast growth of the chromia scale at temperatures above 750 °C produces pores and cracks and which also results in the decohesion of the external oxide scale.

Oxide Evolution with Thermal Cycling

Interrupted cyclic fatigue experiments require cooling of the sample to room temperature before SEM DIC images can be collected and thermal cycling resumed. During the thermal cycle, shown in Fig. 2, the oxide speckle may evolve and the digital image correlation may be lost if the oxide is sufficiently thick to have enough stored energy to drive spallation [45]. This typically occurs when the oxide approaches several microns in thickness [46, 47]. Images were collected from the same location on the surface of the unstrained samples after 12 hours oxidation at 400 °C and 650 °C, and after 1, 2, 3, 5 and 7 thermal cycles. A thermal cycle consisted of sample heating to 400 °C or 650 °C at a rate of 10 °C min^{-1}, followed by a 12 hour hold at temperature, and then cooling to room temperature at a rate of -10 °C min^{-1}. Residual plastic strain measurements were made after the first and seventh temperature cycles, as shown in the maps in Fig. 9(a and b). Image correlation was obtained for all the samples investigated, indicating that the oxide layer did not evolve during the thermal cycles. The total map average ε_{xx} strain shown in Fig. 10(a,c) for all three materials remains between ±0.08%, which is the resolution of the SEM DIC technique used in this investigation for the given parameters, and does not evolve noticeably after the initial 2 or 3 thermal cycles. Furthermore, the strain measurements made at each interrupted thermal cycle show a variability that is commensurate with that of the SEM DIC technique alone, in Fig. 10(b), indicating that the thermal cycles alone do not result in residual strain localization at the sample surface.

The oxide evolution was characterized using thermogravimetric analysis (TGA) to determine the change in mass of samples during thermal cycles for the René 88DT, IN100 and Inconel 718DA. Multiple flat specimens with thicknesses of 800 μm and 13 mm width were analyzed by TGA in order to increase the ratio of oxidized surface to total mass. A total surface area of 2122.56 mm^2 was tested for each TGA measurement in high-purity alumina crucibles. The specimens were heated in air at 650 °C and were allowed to stabilize at this temperature for 45 minutes, before a 10 hours dwell. The measured TGA data was normalized by a subtracted baseline TGA experiment performed without samples present. The TGA data shows the oxidation behavior versus time during isothermal holds at 650 °C for the three alloys. The mass change is shown in Fig. 11 once the temperature stabilized at 650 °C. The TGA data recorded shows significant mass increase during the initial 2 hour period, followed by slow constant growth of the oxide. The parabolic rate in the constant growth regime

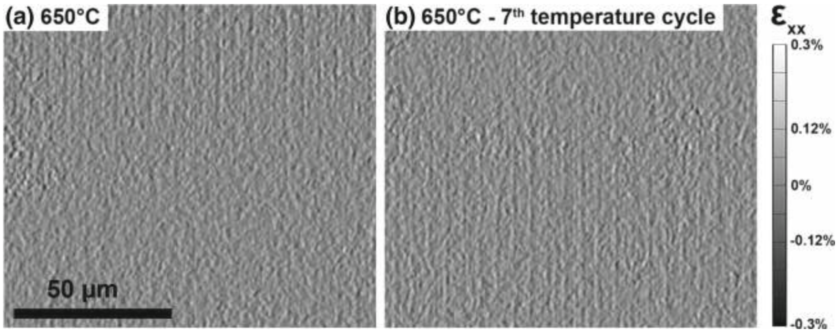

Fig. 9 SEM DIC ϵ_{xx} strain maps for René 88DT thermally cycled once (**a**) and seven times (**b**) at 650 °C with no mechanical deformation showing no residual strain evolution

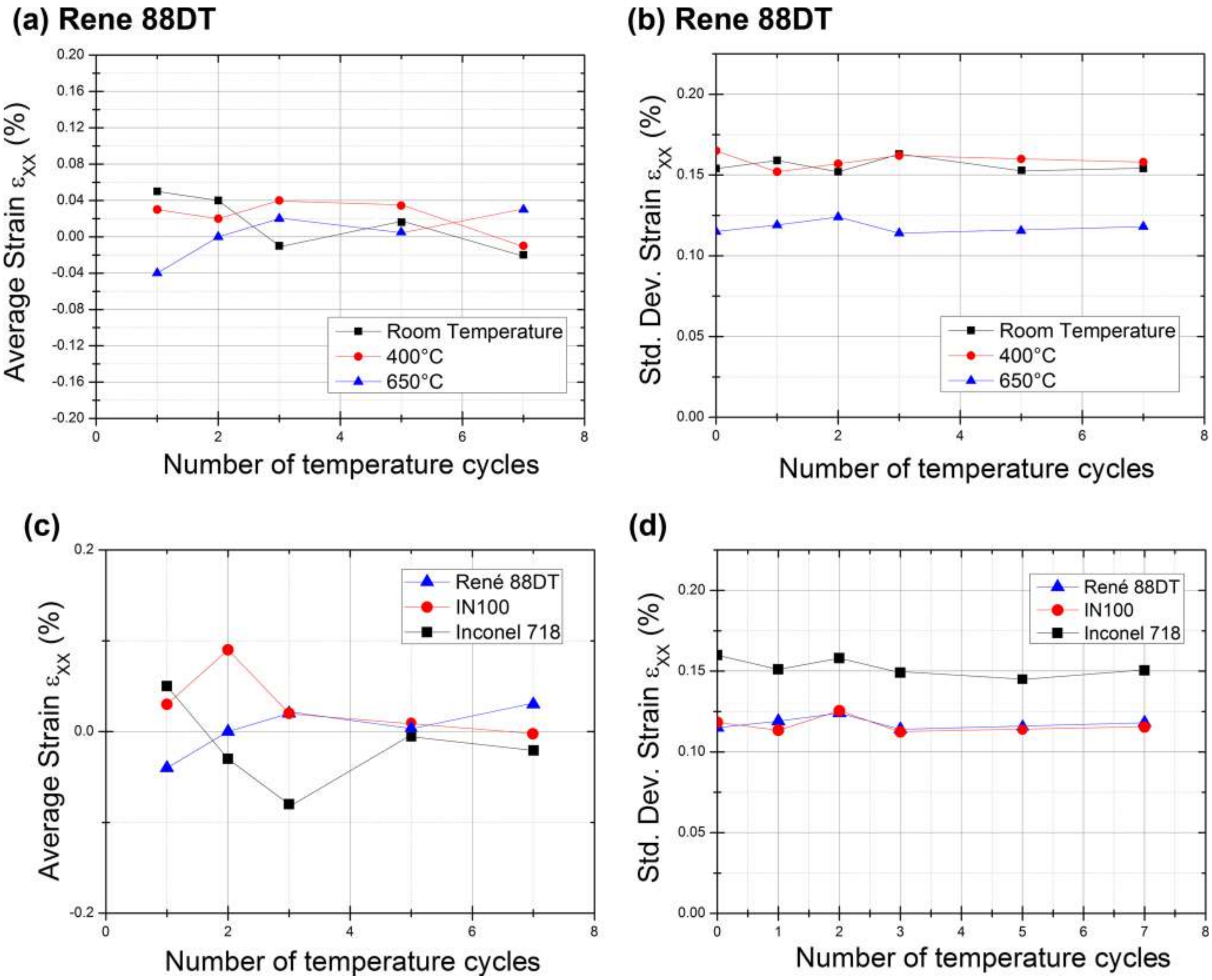

Fig. 10 The average SEM DIC ϵ_{xx} strain measurements and variability in these measurements are shown as a function of thermal cycles for René 88DT at room temperature, 400 °C and 650 °C in (**a**, **b**) and for René 88DT, IN100, and IN718DA at 650 °C (**c**, **d**). The total map average e_{xx} strain shown in Fig. 10(a,c) for all three materials remains between ±0.08% and does not evolve significantly after 2 or 3 thermal cycles

was low, indicating a small change in mass per time, and no significant evolution after the initial 2 hour transient. The predicted oxide layer thickness, based on the mass gain for René 88DT (0.3 mg mass gain), IN100 (0.4 mg mass gain) and Inconel 718DA (0.38 mg mass gain), was calculated using the average density of chromium oxide (5.22 g/cm^3), as 27 nm, 36nm and 32nm, respectively. The calculated oxide layer thicknesses is the same order of magnitude as the observed oxide thicknesses measured by SEM imaging of cross-sectioned oxidized specimens, as shown in Fig. 4(d). The oxide thicknesses observed by FIB cross sectioning were roughly 100 nm. The discrepancy in thickness between these two measurements may arise from the limited accuracy on the TGA measurements and the uncertainty of the value of the chromium oxide density.

Oxide Evolution with Deformation at Temperature

Sub-grain SEM DIC is a surface sensitive technique. The use of the native oxide as a speckle pattern allows for the measurements of displacements in the oxide layer. The oxide was shown to be very thin in Section "Oxide Evolution with Thermal Cycling" and strongly adherent [3, 36, 37, 39–41], therefore deforming uniformly with the superalloy substrate. In order to validate this, DIC measurements were performed on samples subjected to a single deformation cycle to 1% macroscopic deformation at 400 °C and 650 °C. SEM images were collected from the same sample location after oxidization at 400 °C and again after the deformation cycle at 400 °C with 1% applied macroscopic strains and are shown in Fig. 12(a and b). An associated

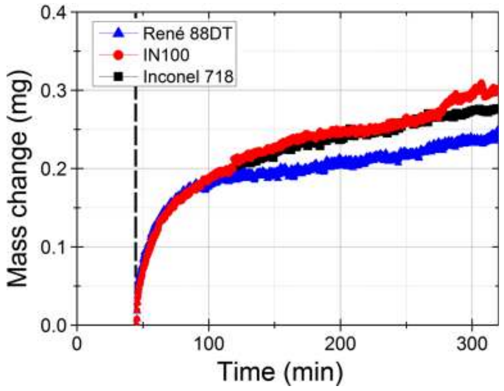

Fig. 11 TGA experiments show the mass change as a function of time at 650 °C, resulting from oxide formation and evolution for the three polycrystalline superalloys. Mass gain occurs at a faster rate over the initial two hour period, while the passivating oxide is formed. The oxidation rate then slows significantly for all three materials

movie in the Supplemental Material Section shows these SEM images, superimposed, before and after deformation. The SEM DIC-measured strain field in Fig. 12(c) shows slip band formation at the surface of the sample after deformation. Discontinuities in the displacement field at the oxide layer surface are observed in Fig. 12(d) and result in the residual strain localization in Fig. 12(c). Therefore, in the plastic regime, shearing by slip band formation at the grain scale occurs during deformation at temperatures up to 650 °C, in a manner similar to that observed at room temperature [26]. Shear is also transmitted into the thin oxide layer making it possible to measure the strain localization along slip bands at a temperature of 650 °C due to the very low toughness of the oxide [48, 49]. FIB-SEM cross sections were made at the exact location of slip bands, Fig. 12(d), showing that the oxide layer is fully adherent to the substrate at the extrusion location.

Oxide Evolution with Cyclic Deformation

Fatigue tests have been performed in the HCF and LCF regime using the oxide as the speckle pattern for SEM DIC measurements. No loss of correlation during LCF cycling was observed before the appearance of damage in the superalloy, observed by SEM. During low cycle fatigue at high temperatures in superalloys, deformation generally occurs by slip with planar precipitate shearing [3] at relatively low numbers of cycles. However during HCF, loss of correlation may occur before the appearance of damage in the superalloy. The loss of correlation is due to a modification of the morphology of the oxide layer in local regions at the sample surface, as shown in Fig. 13(a), where a sample at 79% of the fatigue lifetime was tested in the HCF regime at 650 °C. TEM lamellae were extracted from a region where oxide uplift from the surface was observed, shown in Fig. 13(b and c), which formed where high levels of plasticity occurred, Fig. 13(d and e). Microcracks were also observed in the oxide layer in the locally plastic strained regions, Fig. 14, further degrading the image correlation. Environmental effects manifest at long thermomechanical exposures leading to oxide layer evolution in the HCF regime, including oxide spike formation and microcracking of the oxide [3], limiting the measurement of the strain field by SEM DIC. Strain measurements were made

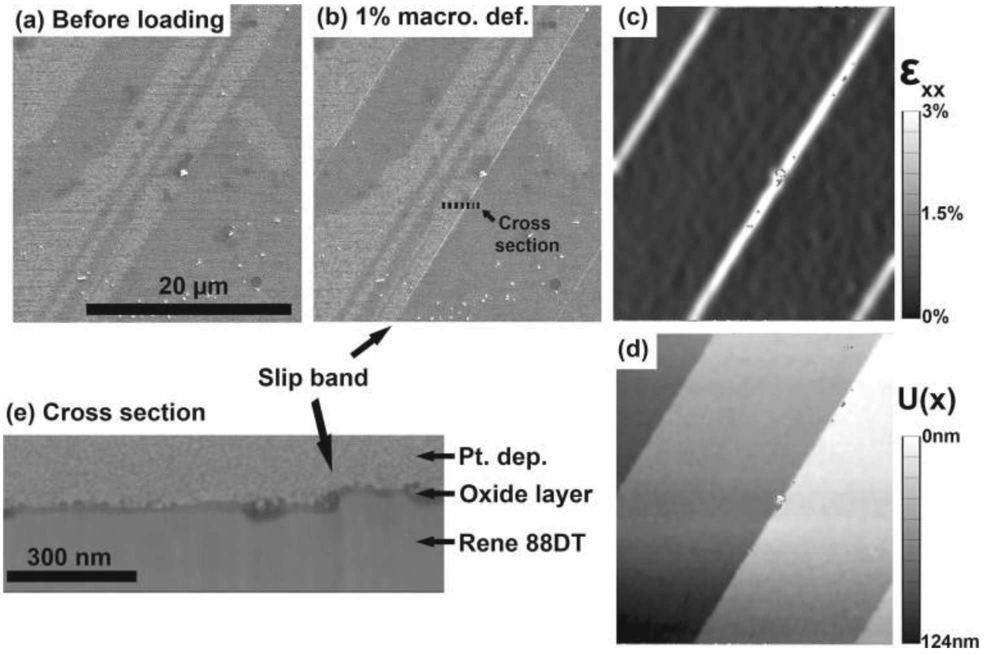

Fig. 12 SEM images were collected from a sample before (**a**) and after (**b**) a single deformation cycle to 1% macroscopic deformation at 400 °C. The SEM DIC strain field ϵ_{xx} (*horizontal to page*) is measured in (**c**) showing residual strain localization along a twin boundary that was FIB-SEM cross sectioned in (**e**), revealing the oxide-substrate interface fully intact along the slip band. The SEM DIC displacement field in (**d**) shows the sharp discontinuity resulting from the slip band

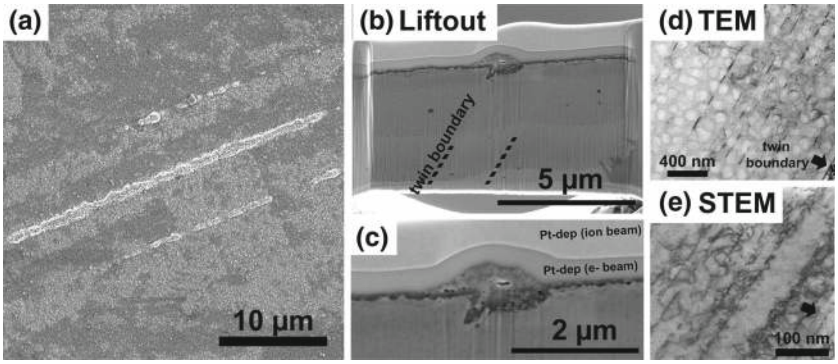

Fig. 13 A René 88DT sample after 79% of expected fatigue lifetime tested in the HCF regime at 650 °C shows oxide spikes forming at the surface (**a**). FIB-SEM cross sections shown the oxide spike forming nearby a twin grain boundary at the surface that has deformed (**b**, **c**). TEM images of this lamellae show high levels of plasticity and slip bands activation parallel to the twin boundary (**d**, **e**).

in the LCF regime where no loss of correlation occurred before the appearance of damage in the superalloy.

Application to Strain Localization during Monotonic Loading

The SEM DIC technique has enabled the measurement of strain heterogeneities introduced by plastic deformation at the μm-scale in René 88DT. Sub-grain DIC measurements have been performed at 20 adjacent regions of interest after tensile loading at 800 MPa, 950 MPa ($\simeq$ 1% macroscopic strain) and 1025 MPa ($\simeq$ 1.5% macroscopic strain) at 650 °C. DIC strain measurements were related to the grain and twin microstructure as determined by EBSD mapping. The strain field ϵ_{xx} is shown with respect to the microstructure for the 20 regions of interest that were stitched together in Fig. 15(b,c and d). Bands of concentrated strain directly correlate with the grain structure. The bands of concentrated strain that occur at early stages of deformation are localized near twin boundaries as indicated with black arrows in Fig. 15(b and c). Moreover, the highest localization at each monotonic loading condition at 650 °C is systematically observed near twin boundaries. For the same macroscopic loading conditions, the amplitude of the strain along a band of concentrated strain observed at 650 °C is lower in comparison to that observed at room temperature [26]. Since strain values measured using SEM DIC depend on the imaging and DIC parameters used when investigating discontinuities such as slip bands [26], all strain maps were obtained with the same imaging and DIC parameters for both room temperature and 650 °C measurements. Interestingly, the number of concentrated strain bands per grain is significantly higher and the band spacing is a smaller at 650 °C, compared to the room temperature DIC measurements.

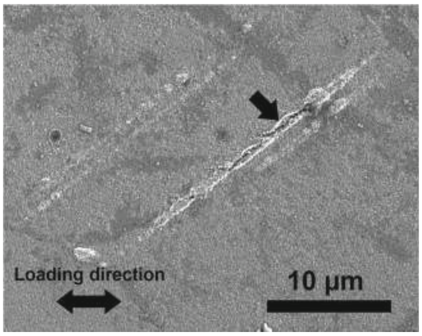

Fig. 14 A René 88DT sample after 82% fatigue lifetime tested in the HCF regime at 650 °C shows oxide spikes at the surface with microcracks forming nearby (at *arrow*)

Application to Strain Localization during Fatigue

Strain Localization during LCF at 650 °C

The SEM DIC technique has enabled the measurement of strain heterogeneities at the μm scale in René 88DT induced by cyclic loading. Sub-grain DIC measurements have been performed at 10 regions of interest after fatigue cycling (R= −1) at 750 MPa, 1000 MPa and after 1% monotonic straining at 650 °C. Local and average DIC strain measurements were related to the grain and twin microstructure as determined by EBSD mapping. The average residual strain measurements by SEM DIC at 10 regions of interest ($\approx$250 grains) are compared to macroscopic strains obtained from a high temperature ceramic extensometer in Table 1. The average SEM DIC strain measurements at 650 °C are within 3% of the macroscopic extensometer strain measurements.

The ϵ_{xx} strain field is shown with respect to the microstructure in Fig. 16(c) after an initial deformation cycle at 750 MPa at 650 °C. The Schmid factor maps for the two potential high temperature slip systems, $\{111\}\langle110\rangle$ and $\{111\}\langle112\rangle$, are given in Fig. 16(a and b). Small amounts of compressive residual strain localization were observed in the first cycle along the $\{111\}$ planes nearby and parallel to the twin boundaries in the grain A1-B1 before yielding, which has a high Schmid factor for the $\{111\}\langle112\rangle$ slip system. For this same sample a second loading cycle was

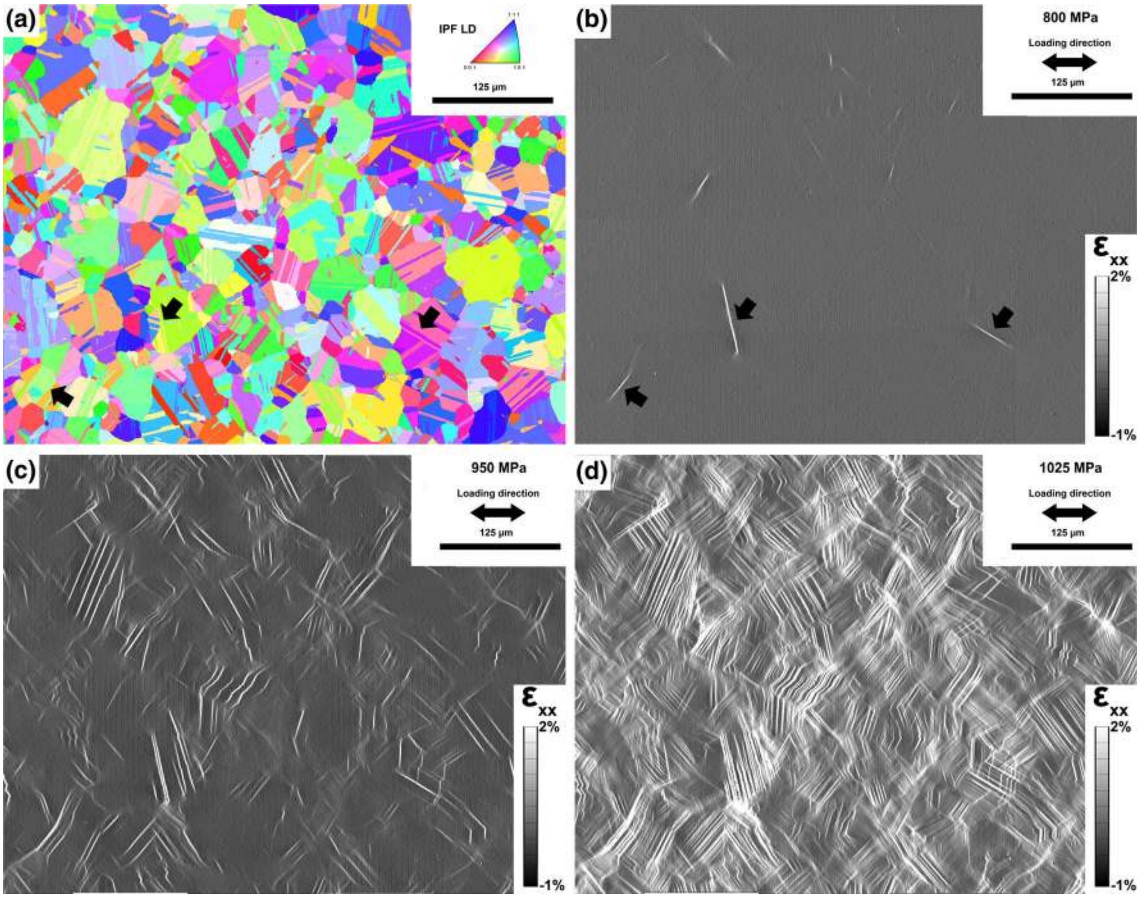

Fig. 15 A René 88DT sample was deformed in tension at 800 MPa (**b**), 950 MPa (**c**) and 1025 MPa ($\simeq$ 1.5% macroscopic deformation) (**d**) at a temperature of 650 °C and then SEM DIC measurements were made. The ϵ_{xx} strain field for each loading condition is shown in (**b**, **c**, **d**). EBSD information collected from the same locations as the measurements in (**b**, **c**, **d**) is shown in (**a**)

performed at 1000 MPa, where yielding occurs, and the ϵ_{xx} strain field was measured, Fig. 16(d). Highly localized bands of concentrated strain occur along twin boundaries or intragranular regions. The highest strain localization is observed along twin boundaries when the bands of concentrated strain are parallel to the twin boundaries. Strain localization occurred either in grains with a high Schmid factor for the $\{111\}\langle 110\rangle$ slip system such as grain A2-B2 or for a $\{111\}\langle 112\rangle$ slip system such as grain A1-B1, indicating that at 650 °C, both slip systems are active and contribute to plastic deformation.

Table 1 The macroscopic residual strain and average strain measured by SEM DIC for René 88DT

	Residual Macro. Strain (%)	Average DIC ϵ_{xx} strain (%)
Room temperature ≈1 % macro. Def. [23]	0.48	0.45
400 °C ≈1 % macro. Def.	0.52	0.51
650 °C ≈1 % macro. Def.	0.65	0.63

Residual strain refers to remaining strain after unloading

Interrupted fatigue tests (R$= -1$) were also conducted at 1000 MPa and 650 °C with sub-grain DIC measurements at 10 regions of interest. Figure 17(a) shows the ϵ_{xx} strain field after 20% of the fatigue lifetime for two regions of interest. The associated Schmid factor maps for both of the potential activated slip systems at 650 °C are given in Fig. 17(b and c). The red boxes inset in the ϵ_{xx} strain maps in Fig. 17(a) show SEM images of the regions from Fig. 17(d and e) after 20% of the fatigue lifetime and near rupture. Significant strain localization occurs along bands nearby and parallel to twin boundaries in large grains with either a high Schmid factor on a $\{111\}\langle 110\rangle$ (grain A4-B4) or a $\{111\}\langle 112\rangle$ (grain A3-B3) slip system. Importantly, strain localization at 20% fatigue life is observed prior to the development of any significant surface offsets (intrusions or extrusions). At 95% of fatigue life, damage of the surface oxide is observed near a twin boundary in Fig. 17(e). Correlation was lost between 20% and 95% life for the high-resolution SEM DIC parameters applied in this investigation, however strain

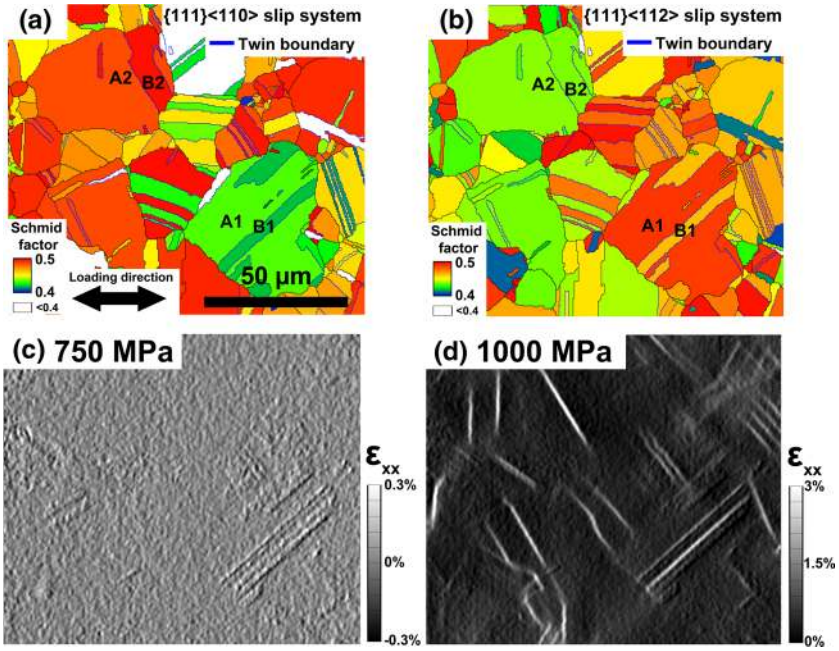

Fig. 16 A René 88DT sample deformed in LCF at 750 MPa (**c**) and 1000 MPa (**d**) with R-ratio of −1 at a temperature of 650 °C for 1 cycle, followed by SEM DIC measurements. The ϵ_{xx} strain field for each loading condition is shown in (**c**, **d**). EBSD information collected from the same locations as the measurements in (**c**, **d**) was used to calculate the Schmid factor (SF) maps for the $\{111\}\langle 110\rangle$ (**a**) and the $\{111\}\langle 112\rangle$ (**b**). Grains A1-B1 have high SF in (**b**) and low SF in (**a**), grains A2-B2 show the opposite trend, though a high degree of strain localization is shown in both grain locations in (**d**) indicating that both slip systems are active

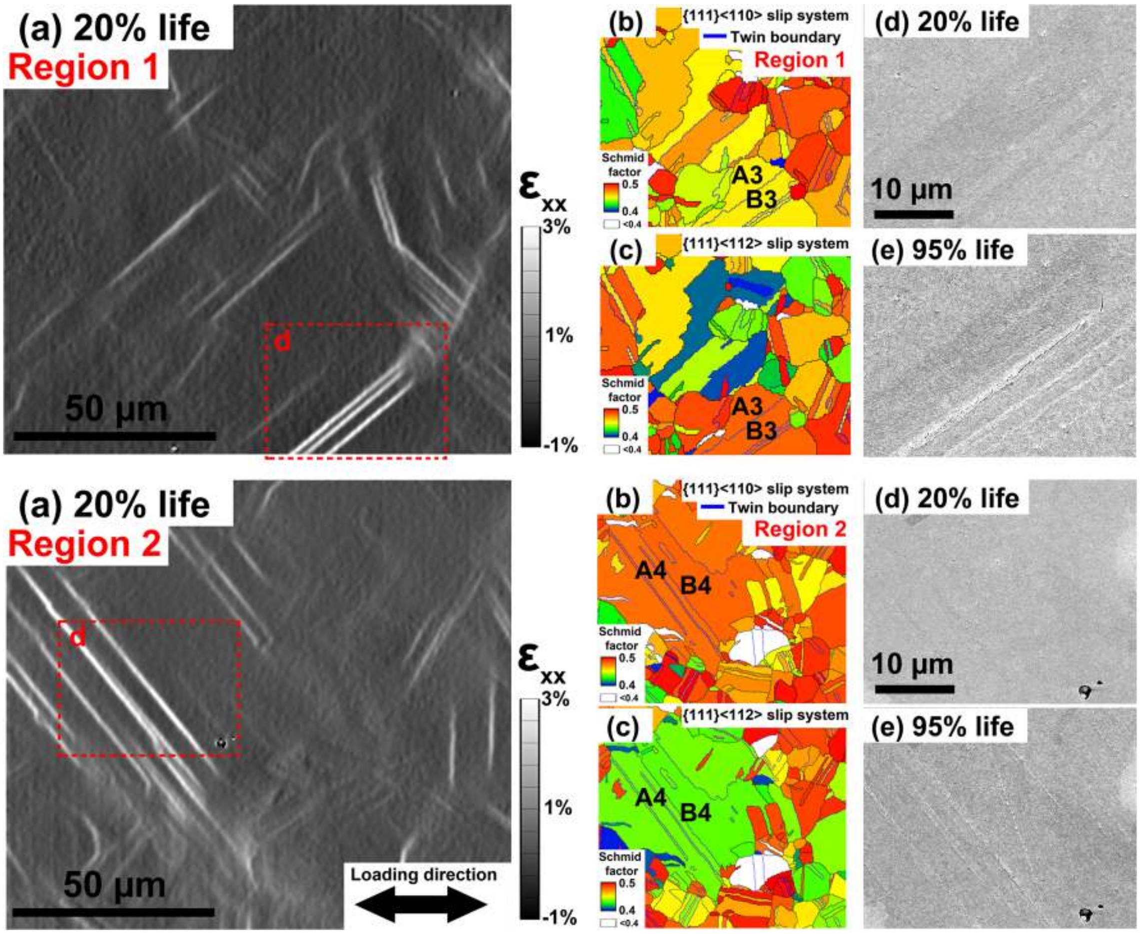

Fig. 17 LCF fatigue experiments were performed to 20% life and SEM DIC ϵ_{xx} measurements were made from different sample locations, two of which are shown in (region 1) and (region 2). The associated $\{111\}\langle 110\rangle$ and $\{111\}\langle 112\rangle$ Schmid factor maps for the region in (**a**) are shown in (**b**, **c**). When comparing the 20% to 95% lifetime SEM images in (**d**) to (**e**), damage is observed in bands parallel and nearby twin boundaries in large grains with high Schmid factor in either the $\{111\}\langle 110\rangle$ (example grain A4-B4) or a $\{111\}\langle 112\rangle$ (example grain A3-B3) slip system

measurements with a coarser speckle or relaxed correlation parameters may be possible, resulting in a limited strain measurement resolution. A detailed study of plastic deformation in René 88DT at high temperature using sub-grain DIC measurements will be discussed in a future article.

The local microstructural configurations were investigated for the regions that had the highest ϵ_{xx} strain localization from 10 investigated regions of interest (≈250 grains). The highest strain localization systematically occurs nearby twin boundaries with a parallel slip configuration [26], which exists when the {111} slip planes of the activated slip systems on one or both sides of the twin boundary are parallel to the twin boundary plane, as reported previously at room temperature [26]. In the case of a fcc material containing coherent twins, the twin boundary is parallel to a {111} slip plane. Therefore, a parallel slip configuration [26] where an activated slip plane is parallel to the twin plane may be present. Without transmission across twin boundaries, dislocations will glide on a highly stressed, twin-parallel slip system, remaining in the original grain near the twin boundary. Heinz and Neumann [50] observed crack initiation in stainless steel at twin boundaries and suggested that elastic anisotropy causes local stress concentrations, strongly supporting glide adjacent to twin boundaries, and leading to enhanced strain localization compared to a grain boundary with oblique slip planes [50]. An activated slip system parallel to a twin boundary (possible with a coherent twin boundary and parallel slip configuration) allows for dislocations to travel relatively long distances unhindered. In addition, if a local elastic modulus mismatch is present near the twin boundary, high local strains and correspondingly high incompatibility stresses at the boundary are created [50]. Crystal plasticity models show that very high stresses occur near twin boundaries in Ni-base alloys in the parallel slip configuration [7, 8]. At room temperature, strain localization has additionally been shown to occur in large grains with relatively high Schmid factor [1, 2, 7, 26, 27, 51, 52].

The twin and parent grain orientations that exhibit the highest shear strain along the activated slip band after 20% of the fatigue lifetime, at room temperature and 650 °C, are shown on a stereographic triangle with respect to the loading direction in Fig. 18(a and b). Blue and red lines connect the twin and parent grains, at room temperature and 650 °C. Iso-curves of the maximum Schmid factors of the {111}⟨110⟩ and {111}⟨112⟩ slip systems are indicated with black dashed curves in Fig. 18(a and b). At room temperature, enhanced strain localization occurs within large grains with high Schmid factors for the {111}⟨110⟩ slip systems. Note that the highest strain localization occurs slightly offset from the maximum Schmid factor location. Previously, we reported that strain localizes at twin and parent grain combinations with relatively high {111}⟨110⟩ Schmid factor and high elastic mismatch [23, 26]. It should be noted that twin and parent grain combinations with the highest Schmid factors systematically have a low elastic modulus mismatch. At 650 °C the highest strain also occurs near twin boundaries with parallel slip configuration between the twin and parent grain pair and at orientations such that the {111}⟨110⟩ Schmid factor is offset from the maximum value. Furthermore, twin and parent grain pairs with orientations that have high {111}⟨112⟩ Schmid factors are also observed to have the highest strain localization. These twin and parent grain pairs have high elastic mismatch, as displayed in Fig. 18(c).

Fracture surfaces of failed fatigue samples at 650 °C were examined by SEM. A detailed study of fatigue initiation in René 88DT at high temperature will be discussed in a future article. For a large number of samples, fatigue cracks leading to failure consisted of large crystallographic facets as displayed in Fig. 19(a,b,c). In low cycle fatigue at R-ratio of −0.5 and at macroscopic stresses of 958 MPa, cracks initiate internally. Lamellae were extracted by FIB-SEM from the faceted surface at the crack initiation sites. The cracks leading to failure were parallel to a twin boundary in all initiation sites investigated. Crystallographic orientation information referenced to the loading direction of the

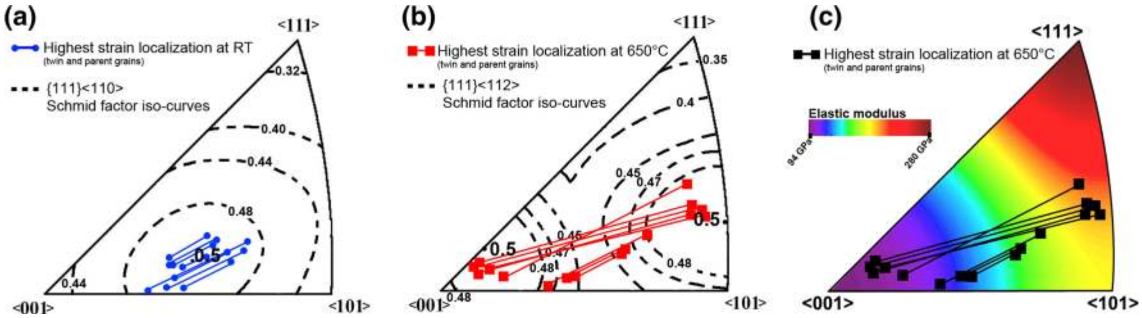

Fig. 18 Twin and parent grain pairs that exhibit the highest strain localization after 20% of the fatigue lifetime, at room temperature and 650 °C, are shown on a stereographic triangle with respect to the uniaxial loading direction and connected with *blue* and *red lines*. Iso-curves of the maximum Schmid factors of the {111}⟨110⟩ and {111}⟨112⟩ slip systems are indicated with *black dashed curves*. **c** Elastic modulus iso-curves are obtained from the compliance matrix of a nickel superalloy at room temperature

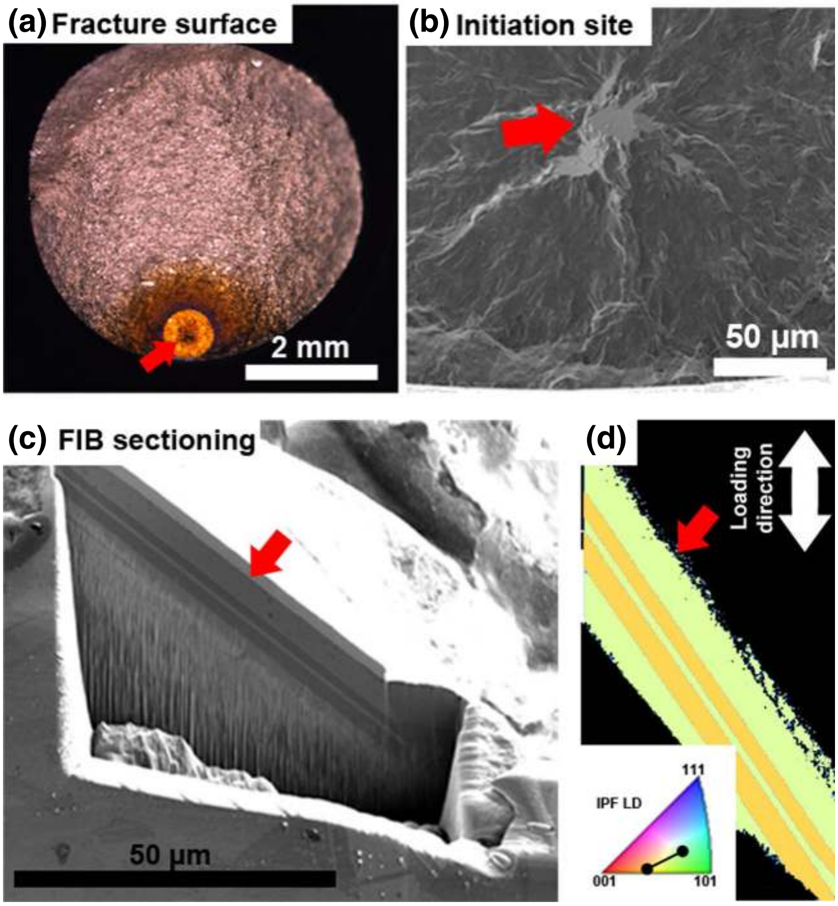

Fig. 19 Subsurface initiation sites for (**a**) a fracture surface from a failed sample deformed at 650 °C. The faceted initiation site is marked with a *red arrow*. A FIB-SEM cross section was used to extract a lamellae from the faceted initiation site, as shown in (**b**, **c**). **d** EBSD measurements were collected from the lamellae to determine the orientation of the parent-twin grain pair that initiated the crack as displayed in insert

twin and the parent grain was extracted for all the investigated initiation sites as displayed in Fig. 19(d) for one specimen. The orientations of four fatigue cracks initiating parent-twin grain pairs are superimposed onto an inverse pole figure (IPF) plot referenced along the loading direction in Fig. 20. Systematically, initiation occurs in parent-twin grain pairs in a parallel slip configuration that have orientations nearby those that exhibit the highest strain localization measured by SEM DIC at the sample surface at 650 °C, which are also shown in Fig. 20. A strong correlation exists between the microstructural configuration that promotes strain localization and crack initiation at 650 °C in LCF.

Oxidation Assisted Processes in the HCF Regime Precluding Strain Localization Measurements

In the HCF regime, the combination of environmental effects and the development of plasticity impact the behavior of the oxide layer. Processes that disrupt the protective oxide scale that lead to the formation of oxide spikes followed by nearby microcracking preclude the measurement of the strain field in these regions. The oxide scale evolves during cycling due to enhanced interaction of oxygen with the slip bands. The oxide uplift that forms during HCF at high stress levels are systematically observed to form near twin boundaries in the René 88DT superalloy, at the same microstructural configurations that lead to extensive strain localization and crack initiation in the LCF regime. This indicates that high levels of plasticity are a primary factor in the development of the disruption of the protective scale followed by oxide spikes formation. In addition oxide

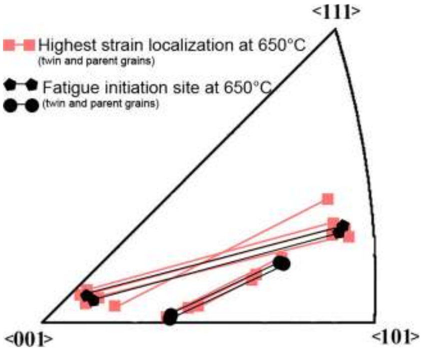

Fig. 20 An IPF map with superimposed parent-twin grain pair orientations connected via lines. In *red*, the orientations of the grain pairs exhibiting the highest strain localization as measured using SEM DIC in LCF. In *black*, the orientations of grain pairs measured from LCF initiated cracks that led to failure when tested at 650 °C

spike formation has not been observed in the HCF regime at low stress. To further investigate the character of these uplifted regions a cross section of an oxide spike was made to image the dislocation sub-structure in a thin lamellae using a SEM STEM detector as shown in Fig. 21(c). A high density of dislocations is apparent near the oxide spike formation site. Interestingly, slip bands parallel and near the twin boundary are observed and influence the development of the oxide formation near twin boundary. It is apparent that the oxide spike forms slightly offset to the twin boundary where slip bands develop during fatigue. Energy dispersive x-ray spectroscopy (EDS) was used with a scanning TEM probe to characterize chemical composition of the oxide spike. Nickel, chromium, oxygen and cobalt EDS

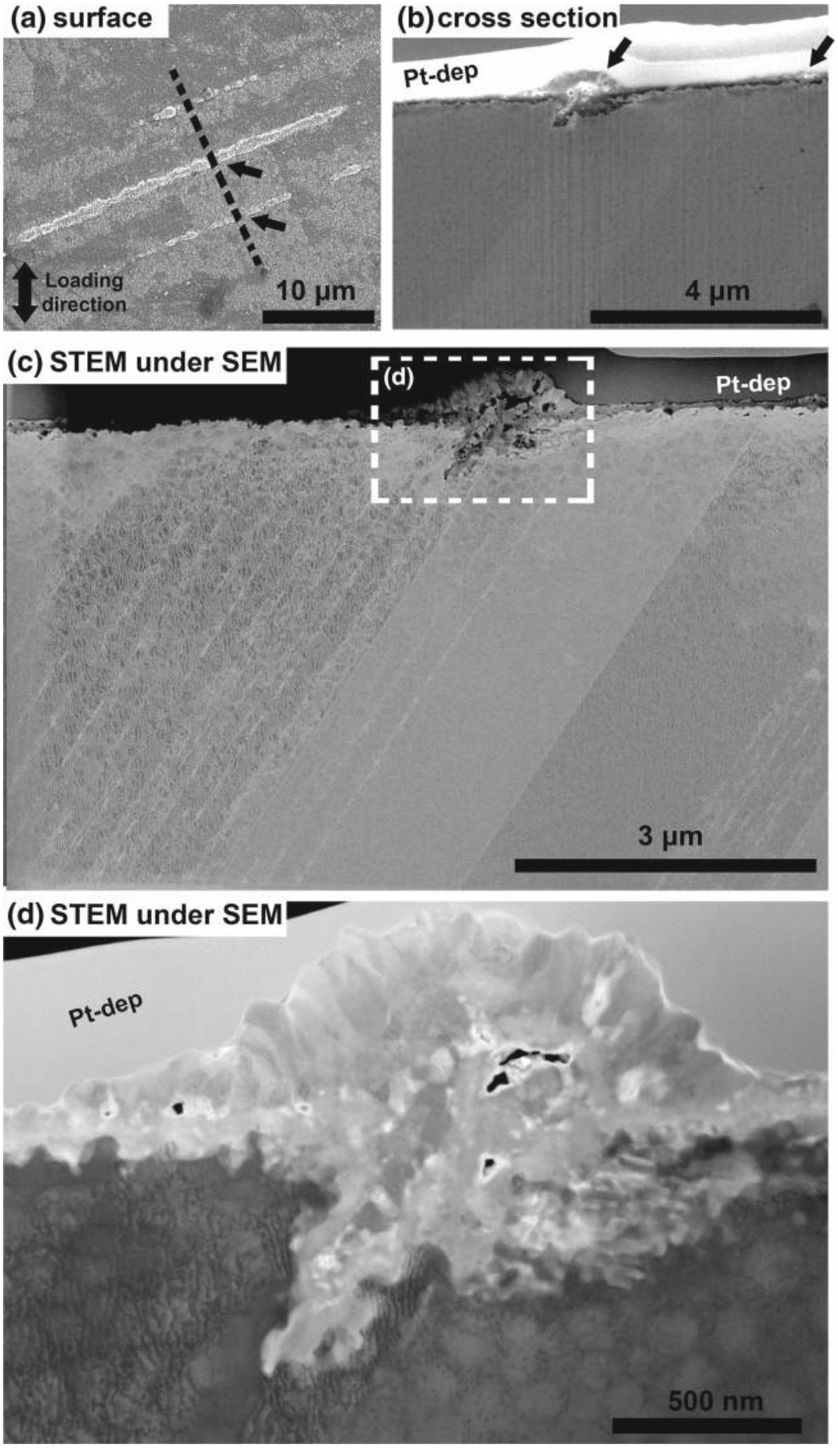

Fig. 21 A René 88DT sample after 79% of expected fatigue lifetime tested in the HCF regime at 650 °C shows oxide spikes forming at the surface in (**a**). FIB-SEM cross sections show the oxide spikes formed nearby a twin grain boundary at the surface in (**b**). SEM STEM images of the lamellae show high levels of plasticity and slip bands activated parallel to the twin boundary where oxide spike formed (**c**). SEM STEM images of the structure of the oxide spike (**d**)

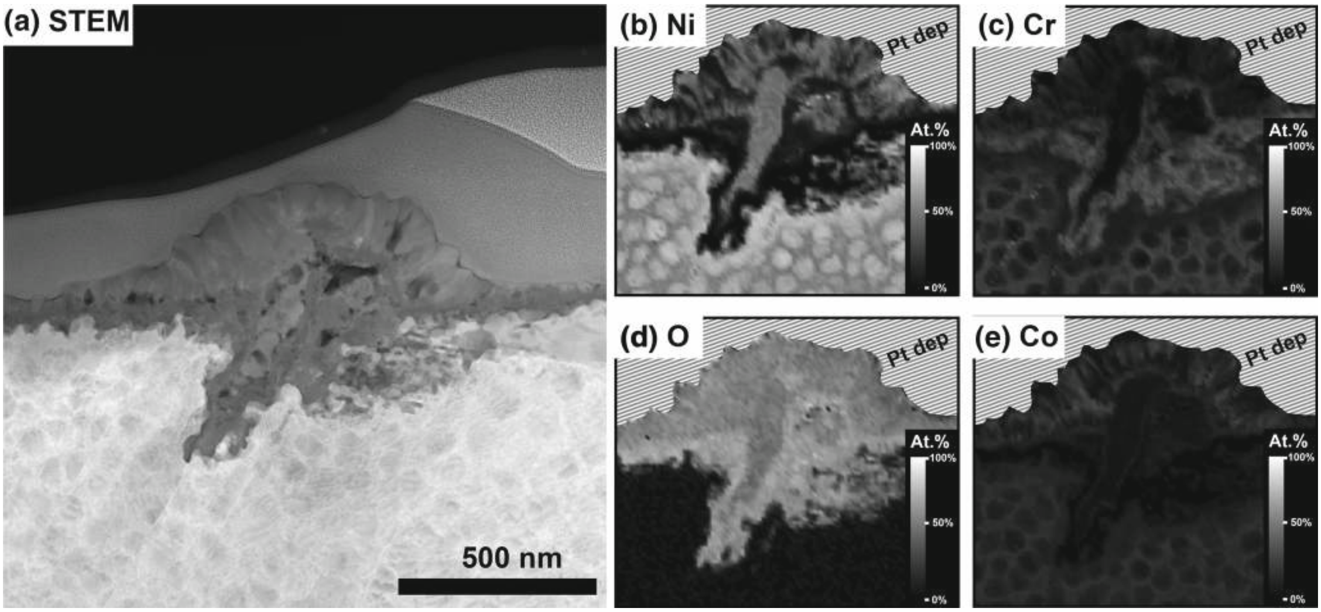

Fig. 22 A René 88DT sample after 79% of expected fatigue lifetime tested in the HCF regime at 650 °C shows an oxide spike forming at the surface by SEM STEM imaging in (**a**). Energy dispersive x-ray spectroscopy maps of the oxide spike are shown in (**b**, **c**, **d**, **e**)

maps are presented in Fig. 22(b,c,d,e) for the oxide spike in Fig. 22(a). Porous nickel (NiO) and cobalt oxide form a columnar structure on the top of the protective chromia scale, indicating that the transport of nickel and cobalt to the surface was likely assisted by dislocation motion. Due to the uncertainty in the quantification of oxygen by EDS, the structure of the cobalt oxide that forms at the surface is unknown, however Co_2O_3 or spinel Co_3O_4 is expected. In addition, a spike of chromia develops under the oxide scale due to diffusion of oxygen from the surface across the

Fig. 23 A René 88DT sample after 79% of expected fatigue lifetime tested in the HCF regime at 650 °C shows a crack at the fatigue specimen surface in (**a**). A cross-section of the crack by FIB-SEM shows the oxide present inside the crack, the precipitate structure, and the slip bands adjacent to the crack in (**b**, **c**)

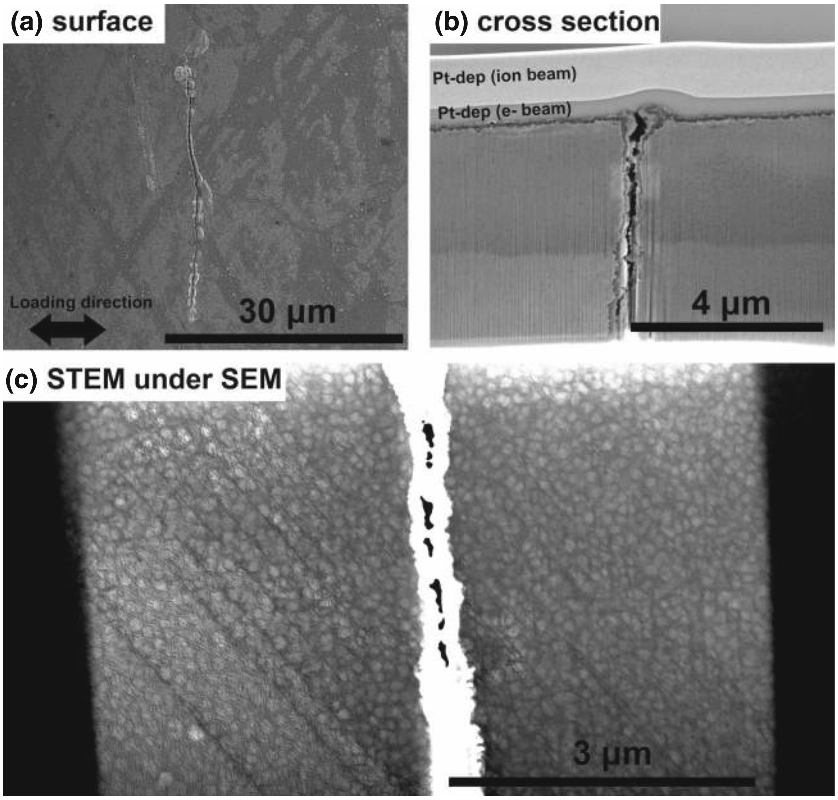

porous nickel and cobalt oxide. After sufficient growth of the oxide spike, local stresses induce fracture of the oxide spike in Fig. 23. Oxygen also diffuses to the metallic substrate at the crack tip, promoting crack growth. The oxygen partial pressure is low at the crack tip, stabilizing the formation of chromia. A schematic showing the mechanisms that operate to form oxide spikes and subsequently crack formation in René 88DT at 650 °C in the HCF regime at high stresses is shown in Fig. 24. The mechanism of the transport of nickel and cobalt to the surface across the protective layer remains to be examined in more detail. Diffusion may occur across the protective layer, or more likely the protective layer is damaged by the slip bands formation which produces channels for transportation of nickel and cobalt through the chormia.

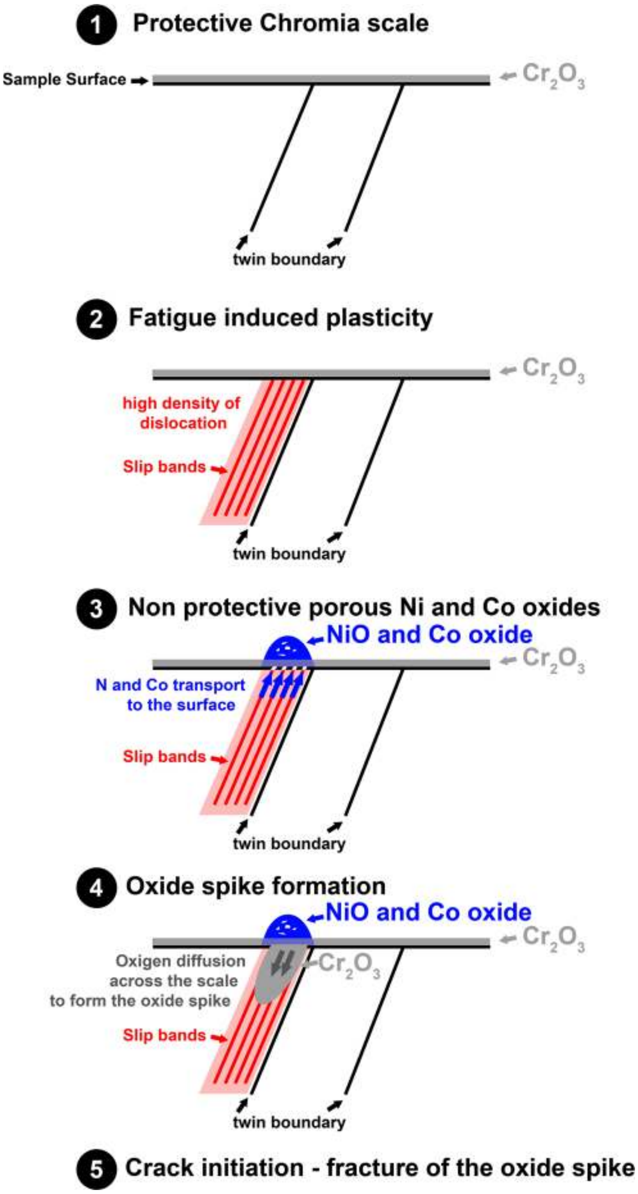

Fig. 24 A schematic showing the mechanisms that operate to form oxide spikes and subsequently crack formation in René 88DT at 650 °C in the HCF regime. A chromia scale is initially present at the sample surface. Upon cycling dislocations accumulate forming slip bands in the regions surrounding preferably orientated twin boundaries along the {111} planes. Dislocation mediated diffusion transports Ni and Co species at the surface to form non-protective porous Ni and Co oxides about the chromia layer. Oxygen diffuses inward producing chromia spike ingress and eventually crack formation

Discussion

The mixed oxide layer that forms with slow growth kinetics on the nickel-base superalloys evolves according to a parabolic rate constant at temperatures below 1000 °C. This results in a low rate of mass gain, after the initial oxide forms during the first few hours of thermal exposure. Khan et al. [53] found that the oxide layer in Inconel superalloys was compact, dense, and adherent after 100 hours at 900 °C, however at temperatures above 1300 °C oxidation becomes catastrophic and deep rivulets appear in the surface. In many Ni and Ni-Fe base superalloys, at thermal exposures below 700 °C where parabolic growth persists (with a very low parabolic rate constant) for extended amounts of time, strain localization can be measured using the high-resolution SEM DIC technique.

In the HCF regime at relatively high stress levels, both the environmental effects and the development of plasticity impact the behavior of the oxide layer. Processes such as the formation of oxide spikes followed by nearby microcracking preclude the measurement of the strain field nearby these features in the René 88DT. In the low stress high cycle fatigue (HCF) regime at intermediate temperatures in nickel base superalloy, damage at the surface is governed by environmental effects that stimulate surface initiation by the oxide assisted processes such as oxide spike formation or grain boundaries embrittlement [3, 54]. In the nickel base superalloy 718DA, enhanced oxidation that occurs at the grain boundary that favors the formation of porous spinels of NiO and FeO [55]. In René 88DT, the disruption of the uniform adherent oxide scale is followed by localized spike formation at slip bands containing high densities of dislocations nearby twin boundaries that present parallel slip configuration [27].

In the LCF regime, strain localization can be observed by SEM DIC due to the extensive plastic deformation that evolves after a low numbers of cycles. Strain accommodated during LCF by slip band formation has been detected via SEM DIC in the surface oxide layers. In superalloys, at temperatures below 700 °C, the oxide is compact, dense, thin and adherent to the substrate, allowing for the measurement of strain using SEM DIC. Shear strains in the superalloy substrate produce shear discontinuities in the oxide layer because of the relatively low oxide toughness [48, 49].

Above 750 °C internal oxidation was observed as shown in Fig. 7. Therefore, the use of the surface oxide layer as a speckle pattern to determine the deformation behavior of the bulk superalloy is not possible, however measurements of the deformation behavior of the surface oxide layer can be obtained.

Conclusions

The strain resolution enabled by the combination of SEM and DIC coupled with the mechanical experiments enables the measurement of strain heterogeneities introduced by cyclic loading at temperatures up to 650 °C at the µm scale. The use of the oxide layer as a speckle pattern permits resolution of the strain localization during monotonic loading or low cycle fatigue at temperatures up to 650 °C in air for several nickel base superalloys. At temperatures above 700 °C, oxidation effects preclude the measurement of strain by DIC. It has been demonstrated that DIC measurements are feasible in a regime where the oxide layer does not evolve during fatigue cycling and where the environmental effects can be neglected. In the René 88DT superalloy, significant strain localization is observed near twin boundaries during low cycle fatigue at 650 °C, correlating with the activation of the $\{111\} < 110 >$ and the $\{111\} < 112 >$ slip system. Also, a strong correlation exists between the microstructural configuration that promotes strain localization during monotonic loading and crack initiation at 650 °C in LCF.

Acknowledgements The authors gratefully acknowledge the support of GE Global Research and appreciate useful discussions with J. Laflen, A. Loghin, J. Marte, D.J. Jorgensen, and S. Daly. Remco Geurts (FEI) is also acknowledged for his microscope scripting contributions. The Air Force Center of Excellence (Grant # FA9550-12-1-0445) is also acknowledged for their support. The Ministère de l'Économie, de la Science et de l'Innovation of Québec is also acknowledged for the grant attributed via the Research Support Program (PSR), Component 4: Support for International Research and Innovation Initiatives (SIIRI) on the "Optimization of functional graded properties for aeronautic applications.

References

1. Miao J, Pollock TM, Jones JW (2009) Crystallographic fatigue crack initiation in nickel-based superalloy rené 88dt at elevated temperature. Acta Mater 57(20):5964–5974. ISSN 1359-6454. http://www.sciencedirect.com/science/article/pii/S1359645409005357
2. Miao J, Pollock TM, Jones JW (2012) Microstructural extremes and the transition from fatigue crack initiation to small crack growth in a polycrystalline nickel-base superalloy. Acta Mater 60(6-7):2840–2854. ISSN 1359-6454. http://www.sciencedirect.com/science/article/pii/S1359645412000870
3. Pineau A, Antolovich SD (2009) High temperature fatigue of nickel-base superalloys – a review with special emphasis on deformation modes and oxidation. Eng Fail Anal 16(8):2668–2697. ISSN 1350-6307. http://www.sciencedirect.com/science/article/pii/S1350630709000259. Special issue honouring Professor Manuel Elices on the occasion of his 70th birthday
4. Viswanathan GB, Sarosi PM, Henry MF, Whitis DD, Milligan WW, Mills MJ (2005) Investigation of creep deformation mechanisms at intermediate temperatures in René 88 {DT}. Acta Mater 53(10):3041–3057. ISSN 1359-6454. http://www.sciencedirect.com/science/article/pii/S1359645405001655
5. Déprés C, Fivel M, Tabourot L (2008) A dislocation-based model for low-amplitude fatigue behaviour of face-centred cubic single crystals. Scr Mater 58(12):1086–1089, 6. http://www.sciencedirect.com/science/article/pii/S1359646208001632
6. Ghosh S, Weber G, Keshavarz S (2015) Multiscale modeling of polycrystalline nickel-based superalloys accounting for subgrain microstructures. Mech Res Commun. ISSN 0093-6413. http://www.sciencedirect.com/science/article/pii/S0093641315001809
7. Cerrone A, Spear A, Tucker J, Stein C, Rollett A, Ingraffea A (October 2013) Modeling crack nucleation at coherent twin boundaries in nickel-based superalloys. In: Materials science and technology (MS&T) conference
8. Stein CA, Cerrone A, Ozturk T, Lee S, Kenesei P, Tucker H, Pokharel R, Lind J, Hefferan C, Suter RM, Ingraffea AR, Rollett AD (2014) Fatigue crack initiation, slip localization and twin boundaries in a nickel-based superalloy. Curr Opin Solid State Mater Sci 18(4):244–252. ISSN 1359-0286. http://www.sciencedirect.com/science/article/pii/S1359028614000370. Slip Localization and Transfer in Deformation and Fatigue of Polycrystals
9. Zhang M, Bridier F, Villechaise P, Mendez J, McDowell DL (2010) Simulation of slip band evolution in duplex ti–6al–4v. Acta Mater 58(3):1087–1096. ISSN 1359-6454. http://www.sciencedirect.com/science/article/pii/S1359645409007198
10. Zhao Z, Ramesh M, Raabe D, Cuitiño AM, Radovitzky R (2008) Investigation of three-dimensional aspects of grain-scale plastic surface deformation of an aluminum oligocrystal. Int J Plastic 24(12):2278–2297. ISSN 0749-6419. http://www.sciencedirect.com/science/article/pii/S074964190800020X
11. Merzouki T, Collard C, Bourgeois N, Zineb TB, Meraghni F (2010) Coupling between measured kinematic fields and multicrystal {SMA} finite element calculations. Mech Mater 42(1):72–95. ISSN 0167-6636. http://www.sciencedirect.com/science/article/pii/S0167663609001562
12. Héripré E, Dexet M, Crépin J, Gélébart L, Roos A, Bornert M, Caldemaison D (2007) Coupling between experimental measurements and polycrystal finite element calculations for micromechanical study of metallic materials. Int J Plastic 23(9):1512–1539, 9. http://www.sciencedirect.com/science/article/pii/S074964190700006X
13. Walley JL, Wheeler R, Uchic MD, Mills MJ (2012) *In-situ* mechanical testing for characterizing strain localization during deformation at elevated temperatures. Exper Mech 52(4):405–416. doi:10.1007/s11340-011-9499-7. ISSN 0014-4851
14. Carroll JD, Abuzaid W, Lambros J, Sehitoglu H (2013a) High resolution digital image correlation measurements of strain accumulation in fatigue crack growth. Int J Fatigue 57(0):140–150. ISSN 0142-1123. http://www.sciencedirect.com/science/article/pii/S0142112312002113. Fatigue and Microstructure: A special issue on recent advances
15. Carroll JD, Clark BG, Buchheit TE, Boyce BL, Weinberger CR (2013b) An experimental statistical analysis of stress projection factors in {BCC} tantalum. Mater Sci Eng A 581(0):108–118.

ISSN 0921-5093. http://www.sciencedirect.com/science/article/pii/S0921509313006515

16. Raabe D, Sachtleber M, Zhao Z, Roters F, Zaefferer S (2001) Micromechanical and macromechanical effects in grain scale polycrystal plasticity experimentation and simulation. Acta Mater 49(17):3433–3441. ISSN 1359-6454. http://www.sciencedirect.com/science/article/pii/S1359645401002427
17. Delaire F, Raphanel JL, Rey C (2000) Plastic heterogeneities of a copper multicrystal deformed in uniaxial tension: experimental study and finite element simulations. Acta Mater 48(5):1075–1087. ISSN 1359-6454. http://www.sciencedirect.com/science/article/pii/S1359645499004085
18. Jin H, Wei-Yang L, Haldar S, Bruck HA (2011) Microscale characterization of granular deformation near a crack tip. J Mater Sci 46(20):6596–6602. doi:10.1007/s10853-011-5608-3. ISSN 0022-2461
19. Kammers AD, Daly S (2013a) Digital image correlation under scanning electron microscopy: Methodology and validation. Exper Mech 53(9):1743–1761. doi:10.1007/s11340-013-9782-x. ISSN 0014-4851
20. Di Gioacchino F, Quinta da Fonseca J (2013) Plastic strain mapping with sub-micron resolution using digital image correlation. Exper Mech 53(5):743–754. doi:10.1007/s11340-012-9685-2
21. Patriarca L, Abuzaid W, Sehitoglu H, Maier HJ (2013) Slip transmission in bcc fecr polycrystal. Mater Sci Eng: A 588(0):308–317. ISSN 0921-5093. http://www.sciencedirect.com/science/article/pii/S0921509313009374
22. Kammers AD, Daly S (2013b) Self-assembled nanoparticle surface patterning for improved digital image correlation in a scanning electron microscope. Exper Mech 53(8):1333–1341. doi:10.1007/s11340-013-9734-5. ISSN 0014-4851
23. Stinville JC, Echlin MP, Texier D, Bridier F, Bocher P, Pollock TM (2015a) Sub-grain scale digital image correlation by electron microscopy for polycrystalline materials during elastic and plastic deformation. Exper Mech 1–20. ISSN 0014-4851
24. Echlin MP, Stinville JC, Miller VM, Lenthe WC, Pollock TM (2016) Incipient slip and long range plastic strain localization in microtextured ti-6al-4v titanium. Acta Mater. submitted
25. Esquivel J, Sangid MD (2015) Digital image correlation of heterogeneous deformation in polycrystalline material with electron backscatter diffraction. Micros Microanal 21:1167–1168, 8. ISSN 1435-8115
26. Stinville JC, Vanderesse N, Bridier F, Bocher P, Pollock TM (2015b) High resolution mapping of strain localization near twin boundaries in a nickel-based superalloy. Acta Mater 98:29–42. ISSN 1359-6454. http://www.sciencedirect.com/science/article/pii/S1359645415004784
27. Stinville JC, Lenthe WC, Miao J, Pollock TM (2016) A combined grain scale elastic–plastic criterion for identification of fatigue crack initiation sites in a twin containing polycrystalline nickel-base superalloy. Acta Mater 103:461–473. ISSN 1359-6454. http://www.sciencedirect.com/science/article/pii/S1359645415007399
28. Jiang J, Zhang T, Dunne FPE, Britton TB (2016) Deformation compatibility in a single crystalline ni superalloy. Proc R Soc A 472
29. Reed RC (2006) The superalloys: fundamentals and applications. Cambridge University Press. ISBN 9781139458634. http://books.google.com/books?id=SIUGcd4a-EkC
30. Krueger DD, Kissinger RD, Menzies RG (1992) Development and introduction of a damage tolerant high temperature nickel-base disk alloy. In: Antolovich SD (ed) Superalloys. Warrendale, PA, pp 277–286. TMS-AIME
31. Miao J, Pollock TM, Jones JW (2008) Fatigue crack initiation in nickel-based superalloy René 88 dt at 593 c. In: Reed RC, Green KA, Caron P, Gabb TP, Fahrmann MG, Huron ES, Woodard SA (eds) Superalloys. Warrendale, PA, pp 589–597. TMS
32. Lenthe WC, Stinville JC, Echlin MP., Pollock T (2016) Statistical assessment of fatigue-initiating microstructural features in a polycrystalline disk alloy. In: 13th International symposium on superalloys, vol 16, page Accepted
33. Texier D, Gómez AC, Pierret S, Franchet J-M, Pollock TM, Villechaise P, Cormier J (2016) Microstructural features controlling the variability in low-cycle fatigue properties of alloy inconel 718da at intermediate temperature. Metallurg Mater Trans A 47(3):1096–1109. doi:10.1007/s11661-015-3291-8. ISSN 1543-1940
34. Milligan WW, Orth E, Schirra J, Savage M (2004) Effects of microstructure on the high temperature constitutive behavior of in 100. Superalloys 331–339
35. Li K, Ashbaugh NE, Rosenberger AH (2004) Crystallographic initiation of nickel-base superalloy in100 at rt and 538 c under low cycle fatigue conditions. Superalloys Champ Pennsy l251–l258
36. Mahesh RA, Jayaganthan R, Prakash S (2008) Oxidation behaviour of selected ni- and fe- based superalloys in air at 900 °C under cyclic conditions. Trans Indian Inst Metals 61(1):45–49. doi:10.1007/s12666-008-0064-8. ISSN 0972-2815
37. Brumm MW, Grabke HJ (1992) The oxidation behaviour of nial-i. phase transformations in the alumina scale during oxidation of nial and nial-cr alloys. Corros Sci 33(11):1677–1690. ISSN 0010-938X. http://www.sciencedirect.com/science/article/pii/0010938X9290002K
38. Cruchley S, Evans HE, Taylor MP, Hardy MC, Stekovic S (2013) Chromia layer growth on a ni-based superalloy: sub-parabolic kinetics and the role of titanium. Corros Sci 75:58–66. ISSN 0010-938X. http://www.sciencedirect.com/science/article/pii/S0010938X13002187
39. Chen JH, Rogers PM, Little JA (1997) Oxidation behavior of several chromia-forming commercial nickel-base superalloys. Oxid Metals 47(5-6):381–410. doi:10.1007/BF02134783. ISSN 0030-770X
40. Greene GA, Finfrock CC (2001) Oxidation of inconel 718 in air at high temperatures. Oxid Metals 55(5-6):505–521. ISSN 0030-770X
41. Wallwork GR, Hed AZ (1971) Some limiting factors in the use of alloys at high temperatures. Oxid Metals 3(2):171–184. doi:10.1007/BF00603485. ISSN 0030-770X
42. Munro M (1997) Evaluated material properties for a sintered alpha-alumina. J Amer Ceram Soc 80(8):1919–1928. doi:10.1111/j.1151-2916.1997.tb03074.x. ISSN 1551-2916
43. Vic-2D (2009) [software]. Correlated Solutions Inc., Columbia
44. Sutton MA, Orteu JJ, Schreier H (2009) Image correlation for shape, motion and deformation measurements: basic concepts, theory and applications. Springer. ISBN 9780387787473. https://books.google.com/books?id=AlkqMxpQMLsC
45. Hutchinson JW, Suo Z (1992) Mixed mode cracking in layered materials. Adv Appl Mech 29(63):191
46. Jackson RW, Lipkin DM, Pollock TM (2014) Thermal barrier coating adherence to hf-modified {B2} nial bond coatings. Acta Mater 80:39–47. ISSN 1359-6454. http://www.sciencedirect.com/science/article/pii/S1359645414005515
47. Jorgensen DJ, Suzuki A, Lipkin DM, Pollock TM (2016) Sulfur and minor element effects on the oxidation of bilayer γ'+ ß bond coats for thermal barrier coatings on rené n5. In: Superalloys 2016: Proceedings of the 13th intenational symposium of superalloys, pp 131–140. Wiley Online Library
48. Pang X, Gao K, Volinsky AA (2007) Microstructure and mechanical properties of chromium oxide coatings. J Mater Res

22:3531–3537. ISSN 2044-5326. http://journals.cambridge.org/article_S0884291400027114

49. Pang X, Gao K, Luo F, Emirov Y, Levin AA, Volinsky AA (2009) Investigation of microstructure and mechanical properties of multi-layer cr/cr2o3 coatings. Thin Solid Films 517(6):1922–1927. ISSN 0040-6090. http://www.sciencedirect.com/science/article/pii/S0040609008012042
50. Heinz A, Neumann P (1990) Crack initiation during high cycle fatigue of an austenitic steel. Acta Metall Mater 38(10):1933–1940. ISSN 0956-7151. http://www.sciencedirect.com/science/article/pii/095671519090305Z
51. Villechaise P, Cormier J, Billot T, Mendez J (2012) Mechanical behaviour and damage processes of udimet 720li: influence of localized plasticity at grain boundaries. In: 12th International symposium on superalloys, pp 15–24
52. Abuzaid WZ, Sangid MD, Carroll JD, Sehitoglu H, Lambros J (2012) Slip transfer and plastic strain accumulation across grain boundaries in hastelloy x. J Mech Phys Solids 60(6):1201–1220. ISSN 0022-5096. http://www.sciencedirect.com/science/article/pii/S0022509612000324
53. Adam Khan M, Sundarrajan S, Natarajan S, Parameswaran P, Mohandas E (2014) Oxidation and hot corrosion behavior of nickel-based superalloy for gas turbine applications. Mater Manuf Processes 29(7):832–839. doi:10.1080/10426914.2014.901530
54. Antolovish SD (2015) Microsctrutural aspects of fatigue in ni-base superalloys. Philosoph Trans A 373
55. Molins R, Hochstetter G, Chassaigne JC, Andrieu E (1997) Oxidation effects on the fatigue crack growth behaviour of alloy 718 at high temperature. Acta Mater 45:663–674